Preprints.org

Article

Not peer-reviewed version

Degradation Mechanism of Methyl Orange Dye Using Fe/Ag/Zn Trimetallic Nanoparticles

Masaku Kgatle * , Keneiloe Khoabane , Gebhu Ndlovu , Nosipho Moloto

Posted Date: 4 November 2025

doi: 10.20944/preprints202511.0036.v1

Keywords: Trimetallic nanoparticles; nanoscale zerovalent iron; Fe/Ag/Zn catalyst; methyl orange dye

Preprints.org is a free multidisciplinary platform providing preprint service that is dedicated to making early versions of research outputs permanently available and citable. Preprints posted at Preprints.org appear in Web of Science, Crossref, Google Scholar, Scilit, Europe PMC.

Copyright: This open access article is published under a Creative Commons CC BY 4.0 license, which permit the free download, distribution, and reuse, provided that the author and preprint are cited in any reuse.

Preprints.org (www.preprints.org) | NOT PEER-REVIEWED | Posted: 4 November 2025 doi:10.20944/preprints202511.0036.v1

Disclaimer/Publisher's Note: The statements, opinions, and data contained in all publications are solely those of the individual author(s) and contributor(s) and not of MDPI and/or the editor(s). MDPI and/or the editor(s) disclaim responsibility for any injury to people or property resulting from any ideas, methods, instructions, or products referred to in the content.

Article

Degradation Mechanism of Methyl Orange Dye Using Fe/Ag/Zn Trimetallic Nanoparticles

Masaku Kgatle [1,*], Keneiloe Khoabane [1], Gebhu Ndlovu [1] and Nosipho Moloto [2]

[1] DSI/Mintek Nanotechnology Innovation Centre, Advanced Materials Division, Mintek, Private Bag X3015, Randburg 2125, South Africa

[2] Molecular Sciences Institute, School of Chemistry, University of the Witwatersrand, P/Bag 3, WITS 2050, Johannesburg, South Africa

* Correspondence: author: MasakuK@mintek.co.za

Abstract

The present study involves the synthesis of polyvinylpyrrolidone (PVP)-stabilized iron-based trimetallic nanoparticles with different metal addition sequences (Fe/Ag/Zn, Fe/Zn/Ag and Fe/(Zn/Ag)) using the sodium borohydride reduction method. In order to investigate the catalytic reactivity of the nanoparticles, a series of batch experiments were performed using methyl orange dye as a model pollutant. It was found that the Fe/Ag/Zn 5:0.1:5 system showed a maximum catalytic activity compared to the other studied trimetallic systems. About 100% of the methyl orange dye was degraded within 1 min and the second-order rate constant obtained was 0.0744 $(mg/L)^{-1}min^{-1}$; the rate of reaction was higher than that of the other trimetallic systems. Furthermore, the effects of pH, initial dye concentration and nanoparticle dosage on the degradation of methyl orange were investigated. The results showed that the reactivity of the Fe/Ag/Zn trimetallic nanoparticles was highly dependent on the aforementioned parameters. Higher reactivity was obtained at lower pH, lower initial methyl orange dye concentration and higher nanoparticle dosage. Lastly, liquid chromatography-mass spectroscopy (LC-MS) was used to elucidate the reaction pathway and identify by-products from methyl orange degradation. The degradation of methyl orange dye using Fe/Ag/Zn trimetallic nanoparticles was rapid; the nanoparticles proved to be effective at degrading methyl orange and can be used to remediate azo-dye wastewater from textile industries.

Keywords: trimetallic nanoparticles; nanoscale zerovalent iron; Fe/Ag/Zn catalyst; methyl orange dye

1. Introduction

The textile industry has been having an inordinate negative effect on the worldwide economic growth as it uses high quantities of water thereby leading to significant pressure on natural water resources [1]. Approximately 10 000 different types of dyes are used in the textile industry and 10-15% are lost in the dyeing processes [2]. Dye concentration values reported in textile industry effluents vary depending on the type of the industry; for instance, 10-800 mg/L [3–5]. Some of these dyes are difficult to remove from the aqueous phase due to their high solubility [2]. The effluent released from textile industries contains a mixture of dyes, metals and other pollutants [6,7]. Moreover, textile wastewater is usually categorized by high chemical oxygen demand (COD), biological oxygen demand (BOD), total organic carbon (TOC), colour and salt content [8,9].

Dyes can generally be classified as either natural or synthetic [6]. Synthetic dyes are further categorized into different groups according to their chemical structures (such as azo, sulphur and anthraquinone types) and their application methods [10]. Among these, azo dyes containing the characteristic azo linkage (–N=N–) are the most extensively used in the textile industry. However, many azo dyes are carcinogenic and mutagenic, posing risks to human and aquatic life due to the ineffectualness of conventional water treatment plants and wastewater treatment strategies in

© 2025 by the author(s). Distributed under a Creative Commons CC BY license.

Preprints.org (www.preprints.org) | NOT PEER-REVIEWED | Posted: 4 November 2025 doi:10.20944/preprints202511.0036.v1

eliminating the colour and mutagenic properties of some dyes [11–13]. Furthermore, azo dye compounds are recalcitrant to biodegradation and persist in the environment due to their high stability which is intended to meet consumer market demands regarding the longevity of colours in the fibres [14].

Traditional techniques for removing textile dyes from water include physical (e.g., sedimentation, flotation, filtration), chemical (e.g., ozonation, chlorination, ion exchange), and biological processes (e.g., aerobic and anaerobic digestion) [15]. However, these approaches have their own drawbacks and shortcomings. The biological methods are said to be time-consuming and have lower efficiencies compared to other methods [16]; while physical treatments merely transfer pollutants between phases without achieving complete degradation [17]. Moreover, none of these methods fully mineralize the contaminants, frequently leading to secondary pollution [18]. To overcome these shortcomings, nanotechnology-based methods have been explored. Nanoparticles composed of transition metals such as Fe and Zn have been widely investigated for the treatment of various pollutants such as organic dyes [19,20], heavy metals [21], chlorinated solvents [22]. Despite their advantages, monometallic nanoparticles often suffer from limited catalytic efficiency and stability. To address these drawbacks, researchers have developed multimetallic systems comprising two or more distinct metals to enhance reactivity and durability [23].

For example, Fe and Zn have been combined to form Fe/Zn bimetallic nanoparticles that effectively degrade organic pollutants [16,24]. Similarly, nanoscale zerovalent iron (nZVI) has been coupled with other metals such as Ag, Pd, Ni or Pt to improve catalytic activity in wastewater treatment [25,26]. These bimetallic systems have been widely applied for the degradation of organic dyes in aqueous media, demonstrating enhanced degradation and adsorption efficiencies compared to their monometallic counterparts [24,25,27]. Wang and co-workers [27] synthesized Fe/Cu bimetallic nanoparticles and they observed greater degradation rates for Orange II dye using the bimetallic Fe/Cu nanoparticles compared to nZVI alone. Gautam et al. [24] demonstrated that Fe/Zn nanoparticles effectively removed malachite green and Congo red dyes in water, with performance strongly influenced by solution pH.

Although bimetallic nanoparticles have proven effective, trimetallic systems represent an emerging research frontier. Unlike monometallic and bimetallic nanoparticles, trimetallic nanoparticles are composed of three different metals, offering unique properties due to the synergistic interactions among their constituent elements. Their unique metal combination enhances catalytic efficiency, conductivity, optical properties, and magnetism, while their core–shell structure improves stability, selectivity, and activity [28,29]. Previous studies have shown that trimetallic nanoparticles display superior catalytic performance compared to their bi- and monometallic analogues [28,30,31]. For instance, Basavegowda and co-workers [28] prepared Fe/Ag/Pt particles that displayed a better catalytic activity in the reduction of p-nitroaniline and decolorization of rhodamine-B when compared to the monometallic (Fe, Ag and Pt) and bimetallic (Fe/Ag and Fe/Pt) nanoparticles. Moreover, Khan [30] reported that Fe/Ag/Pd nanoparticles exhibited excellent catalytic dehydrogenation of formic acid. In our earlier work [32], we reported on Fe/Cu/Ag trimetallic nanoparticles which demonstrated significantly higher catalytic activity for methyl orange degradation than corresponding bimetallic systems.

In this study, nZVI-based trimetallic nanoparticles with low cost and high reactivity were developed. While Fe/Zn and Fe/Ag bimetallic nanoparticles have previously shown promising catalytic activity [24,26], Zn's strong reducing nature can cause rapid oxidation, and Ag's high cost limits large-scale applications. To address these challenges, this research introduces a novel approach by designing trimetallic nanoparticles with varying metal configurations (Fe/Zn/Ag, Fe/Ag/Zn, and Fe/(Zn/Ag)) incorporating minimal silver content. The work further delves into the parametric effects of the Fe/Ag/Zn system in the catalytic degradation of methyl orange dye in aqueous media, opening new doors for efficient and sustainable water treatment solutions. This innovative approach not only addresses the limitations of existing systems but also promises to revolutionize environmental remediation methods with cost-effective and high-performance nanomaterials.

© 2025 by the author(s). Distributed under a Creative Commons CC BY license.

Preprints.org (www.preprints.org) | NOT PEER-REVIEWED | Posted: 4 November 2025 doi:10.20944/preprints202511.0036.v1

2. Experimental

2.1. Reagents

The following chemicals were used for nanoparticle synthesis: iron sulphate heptahydrate ($FeSO_4.7H_2O$, ≥ 99.0%), sodium borohydride ($NaBH_4$, ≥ 98.0%), polyvinylpyrollidone (PVP, MW 40 000), ethanol (99.9%), zinc acetate dihydrate ($Zn(C_2H_3O_2)_2.2H_2O$), hydrochloric acid (HCl, 37.0%) and sodium hydroxide pellets (NaOH, ≥ 98.0%) were all obtained from Sigma Aldrich, South Africa. The silver nanoparticles precursor: silver nitrate ($AgNO_3$, >99.5% purity) was obtained from the Radchem laboratory supplies. Methyl orange dye was obtained from ACE Chemicals. All the chemicals and materials were used as received. Deionized water was used throughout the entire experimental process.

2.2. Nanoparticle Synthesis and Characterization

2.2.1. Synthesis of Nanoparticles

The trimetallic nanoparticles, prepared with varying metal addition sequences, were synthesized using the sodium borohydride reduction method. A typical synthesis involved adding 2 g of PVP, 50 mL of ethanol, and 50 mL of deionized water into a three-neck flask equipped with a magnetic stirrer. The solution was then degassed with nitrogen to remove oxygen and maintain an inert environment for nanoparticle formation. After 30 min, $FeSO_4.7H_2O$ was added into the mixture and stirred for a further 30 min. A solution of $NaBH_4$ was then added dropwise to the $FeSO_4{\cdot}7H_2O$ mixture under vigorous stirring, resulting in the formation of black nZVI nanoparticles. Subsequently, a solution of $AgNO_3$, $Zn(C_2H_3O_2)_2{\cdot}2H_2O$, or both, depending on the desired trimetallic composition, was introduced into the nZVI suspension with continued stirring for 30 min. Then a solution of $NaBH_4$ was added into the mixture in a dropwise manner. The reaction was stopped after 30 min for the Fe/(Zn/Ag) 5:(5:0.1) system. However, for Fe/Ag/Zn 5:0.1:5 and Fe/Zn/Ag 5:5:0.1 systems, after 30 min, Zn $(C_2H_3O_2)_2.2H_2O$ and $AgNO_3$ were respectively added into the reaction vessel. Thereafter, a solution of $NaBH_4$ was added into the mixture in a dropwise manner. Upon stirring for a further 30 min, the nanoparticles were removed from the stirrer and subsequently placed into centrifuge tubes. The nanoparticles were washed in ethanol and dried overnight under vacuum at 25ºC. The summary of the sequence of the addition of nanoparticle precursors is shown in Figure 1.

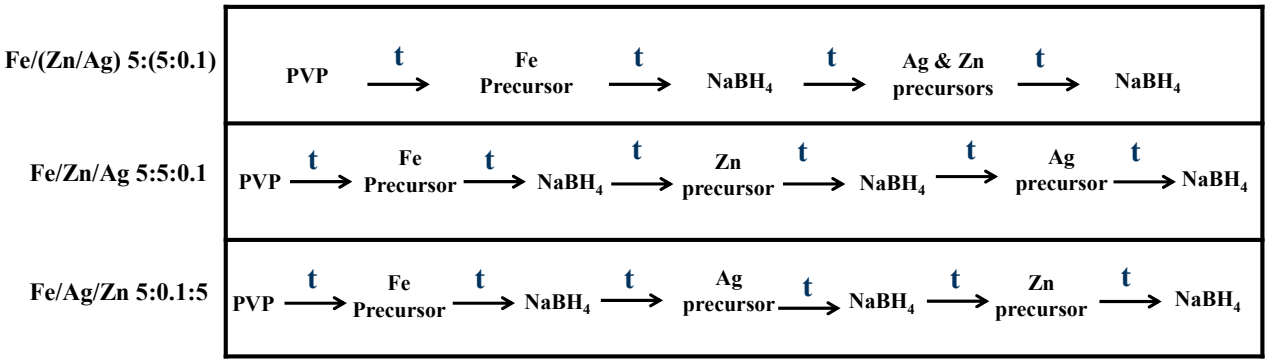

Figure 1. Summary of the nanoparticles' synthesis procedure (t represents time=30 min).

2.2.2. Characterization of Nanoparticles

Transmission electron microscopy (TEM) and energy dispersion X-ray spectroscopy (EDX) were performed on a JEOL JEM-2100F field emission electron microscope. The nanoparticles were suspended in ethanol by ultrasonication and subsequently drop-casted on a 300 mesh formvar coated nickel grid from SPI supplies.

© 2025 by the author(s). Distributed under a Creative Commons CC BY license.

Preprints.org (www.preprints.org) | NOT PEER-REVIEWED | Posted: 4 November 2025 doi:10.20944/preprints202511.0036.v1

Scanning electron microscopy images were obtained using Zeiss Ultra 55 field emission. Images were captured using electron high tension: 2kV, scan speed: 9 times per second and working distance: 2.3-2.4 mm.

The powder X-ray Diffraction (p-XRD) analysis of all samples was conducted on Bruker AXS D8 X-ray advanced powder diffractometer. The XRD was fitted with a LinxEye detector and nickel filter; using the Co Kα (1.78897 Å) wavelength operated at 40 kV and 35 mA. XRD patterns were recorded with a step size of 0.02˚/s in the 2θ range of 0 to 100° diffraction angle. In addition, XRD data was used to approximate the sizes of the particles using the Scherrer equation:

$$D = \frac{K\lambda}{\beta Cos\theta} \quad (1)$$

where, D is the size of the particle, K is the shape factor, λ is the wavelength of radiation expressed in nanometres, θ is the angle of diffraction of the peak in radians and β is the full width at half maximum of the peak expressed in radians [33].

The X-ray photoelectron spectroscopy (XPS) analysis of the trimetallic nanoparticles was conducted using a Thermo Fisher Scientific ESCAlab 250Xi with an Al kα light source at 1486.7 eV running at 300 W of power to identify individual elements in the nanoparticles. The hemispherical electron energy analyzer with a spot size of 900 µm worked in the constant analyzer energy (CAE) mode at an analyzer pass energy of 100 eV for the survey spectra and 20 eV for the high-resolution spectra of each element.

2.3. Methyl Orange Degradation Tests and Analysis

Batch experiments of methyl orange (MO) dye degradation were carried out to measure the catalytic activity of the synthesized nanoparticles. All experiments were conducted in an open-batch system at room temperature. About 50 mL of 10 mg/L MO dye solution was placed in a beaker equipped with a magnetic stirrer bar and stirred on a magnetic stirrer plate at 250 rpm for 30 min. This was followed by addition of 10 mg of the nanoparticles and continued stirring at 250 rpm. Aliquots were drawn into small centrifuge tubes at the following time intervals: 1, 2, 3, 4, 5, 10, 15, 20 and 30 min. These were then quickly centrifuged for 10 min at 12 000 rpm to separate the nanoparticles from the liquid. Parametric tests were conducted by varying the pH, nanoparticle dosage and initial MO concentration. The pH of the solution was varied from 3-12 using HCl and NaOH to adjust, the nanoparticle dosage was varied from 4-10 mg and the initial MO concentration ranged from 10-300 mg/L. The tests were performed under the same experimental conditions as above. The samples were analysed using a Thermo Fisher Scientific, Multiskan GO, UV-vis Microplate Spectrophotometer. The degradation efficiency was calculated using the following equation:

$$\text{Degradation (\%)} = \frac{A_0 - A_t}{A_0} \times 100 \quad (2)$$

where A_0 is the MO dye absorbance before degradation and A_t is the MO dye absorbance at particular time intervals t. The reactivity of surface sites of each of the trimetallic nanoparticles was determined using turnover number (TON) and turnover frequency (TOF). The TON was calculated using the number of active sites as follows:

$$TON = \frac{(DE\%)(moles\ of\ dye)}{Number\ of\ active\ sites\ (moles)} \quad (3)$$

where, DE is the dye degradation efficiency. TOF which is the number of MO dye molecules that one catalytic site can convert into a product [34], was calculated at 5 min reaction time using the following equation:

© 2025 by the author(s). Distributed under a Creative Commons CC BY license.

Preprints.org (www.preprints.org) | NOT PEER-REVIEWED | Posted: 4 November 2025 doi:10.20944/preprints202511.0036.v1

$$TOF = \frac{TON}{time} \quad (4)$$

2.4. Kinetic Study

The kinetic study of the degradation of MO was conducted using the zeroth-, first- and second-order kinetic models. The following differential rate equations were used to define the zeroth-, first- and second order kinetic models, respectively:

$$-\frac{dC_t}{dt} = k_0 \quad (5)$$

$$-\frac{dC_t}{dt} = k_1 C_t \quad (6)$$

$$-\frac{-dC_t}{dt} = k_2 (C_t)^2 \quad (7)$$

where t is the reaction time and C_t is the dye concentration at time, t. Moreover, k_0, k_1 and k_2 are the apparent rate constants of the zeroth-, first- and the second-order kinetic models. The integration of equations (5-7) yields the following equations (8-10), respectively:

$$C_t = C_0 - k_0 t \quad (8)$$

$$C_t = C_0 e^{-k_1 t} \quad (9)$$

$$\frac{1}{C_t} = \frac{1}{C_0} + k_2 t \quad (10)$$

where C_0 is the initial dye concentration. The linear equation of the first-order kinetic model integrated equation (9) is as follows:

$$lnC_t = lnC_0 - k_1 t \quad (11)$$

The rate constants for all the kinetic models were determined from the slope of their linear plots.

2.4.1. Analysis of Methyl Orange Degradation Products and Pathway

The analysis of MO dye and its degradation products was conducted on a Bruker Compact Q-TOF high-resolution mass spectrophotometer. Separations were achieved utilizing a Luna Omega 1.6 µm C18 column (50 × 2.1 mm) and a mobile phase composed 0.1% formic acid, in both acetonitrile and water under isocratic conditions; with a flow rate of 0.3 mL/min. A 20 µL volume of sample was injected using the autosample system. The MS was coupled with an electrospray ionization source (ESI) and operated at positive polarity. The ESI conditions were as follows: capillary voltage= 4500 V, endplate offset= -500 V, nebuliser pressure= 1.8 bar, drying gas flow= 9.0 L/min, temperature= 220 ºC and the mass range 50-1300 m/z.

3. Results and Discussion

3.1. Characterization of the Catalyst

The XRD results of synthesized trimetallic nanoparticles (Fe/Zn/Ag 5:5:0.1, Fe/(Zn/Ag) 5:(5:0.1) and Fe/Ag/Zn 5:0.1:5) are presented in Figure 2. The XRD patterns of the trimetallic nanoparticles depicted the presence of peaks at the 2θ of 45.0º and 66.0º corresponding to nZVI indexed at (110) and (200) crystalline planes, respectively. Iron oxide (Fe_2O_3 and Fe_3O_4) peaks appear at 2θ values of 12.0°, 20.0°, 22.5°, 24.9°, 26.0°, 30.3°, 34.0° and 62.5° [35,36]. The presence of these iron oxide peaks in the nanoparticles provide evidence of the nZVI layered structure, which comprises of a body-

© 2025 by the author(s). Distributed under a Creative Commons CC BY license.

Preprints.org (www.preprints.org) | NOT PEER-REVIEWED | Posted: 4 November 2025 doi:10.20944/preprints202511.0036.v1

centered cubic α-Fe core covered by an oxide shell [35,37]. The existence of oxide peaks in nZVI-based nanoparticles is not a foreign phenomenon as it was also observed in previous studies [26,31,38–40]. The iron oxide might have been formed during the process of nanoparticle synthesis, nanoparticle drying or storing before the nanoparticles could be analyzed [26,38]. Furthermore, Zhou et al. [39] presented evidence of increasing iron oxide intensity in the bimetallic Fe/Pd nanoparticles as they age. However, Yuan et al. [31] showed that although the nanoparticles had moderately oxidized, the prepared Fe/Cu/Ag trimetallic nanoparticles were still highly effective in the degradation of p-nitrophenol and the corrosion products did not accrue on the surface of the trimetallic nanoparticles. This demonstrated that the presence of Cu and Ag on the surface of nZVI could impede its passivation and increase its lifespan.

The Fe^0 peak intensity at 2θ of 45.0º in all trimetallic nanoparticles spectra decreases and widens as compared with the standard Fe XRD pattern. According to studies, the broadening of peaks is due to the reduction of the particle size and stabilization of the nanomaterial [41,42]. A smaller particle size of the crystals increases the number of defects in the crystalline network due to the reduced number of atoms available for crystallite assembly, leading to diffraction peaks with lower intensity and widening [41]. Moreover, the small peak at the 2θ value of 37.5º corresponding to the (111) crystalline plane indicates the presence of pure Ag [43]. The peaks at 2θ values of 34.4º, 39.6º, 53.5º and 71.9º correspond to pure hexagonal Zn. The ZnO peak can be observed at 2θ value of 33.5º [44,45]. Like Fe, Zn (E^o= -0.76 V) is also prone to oxidation but has a lower reduction potential than Fe (E^o= -0.447 V) [46]; which makes Zn more reactive than Fe [22]. Gautam et al. [24] prepared Fe/Zn bimetallic nanoparticles and the XRD results showed the presence of Fe and ZnO. The findings reveal that alongside oxide phases, Fe, Zn, and Ag coexist within the trimetallic nanoparticles while maintaining their individual crystalline structures. All three samples display similar crystalline features, although the Ag peaks are weak or nearly invisible owing to the small amount of silver present. The crystallite sizes determined by the Scherrer equation using all high intensity XRD peaks of the Fe/Ag/Zn, Fe/Zn/Ag and Fe/(Zn/Ag) nanoparticles were 18.9, 21.5 and 23.2 nm, respectively.

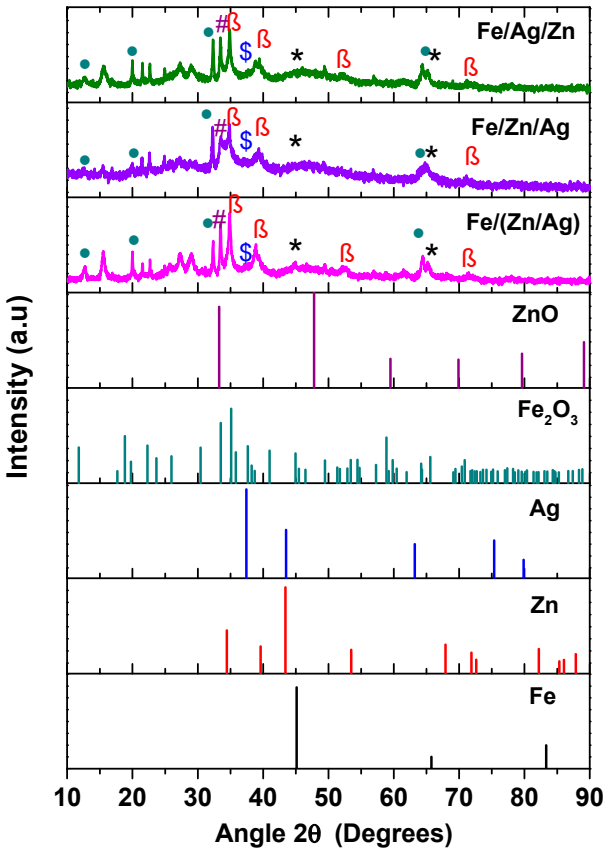

© 2025 by the author(s). Distributed under a Creative Commons CC BY license.

Preprints.org (www.preprints.org) | NOT PEER-REVIEWED | Posted: 4 November 2025 doi:10.20944/preprints202511.0036.v1

Figure 2. X-ray diffraction (XRD) patterns of the trimetallic nanoparticles and standard XRD plots of Fe, Zn, ZnO and Fe_2O_3. (Peaks of Fe^0: *, peaks of Fe_2O_3: ●, peaks of Ag: $, peaks of Zn: β and peaks of ZnO: #).

Figure 3 shows the EDX spectra of the synthesized trimetallic nanoparticles, which confirms their elemental composition. The EDX spectra show the presence of the main elements Fe at 0.7, 6.4 and 7.2 keV, Ag at 3.0 keV, Zn at 8.6 and 9.5 keV and O at 6 keV, as also observed in the XRD patterns. The presence of O in the spectra indicates that there were oxides co-existing with the trimetallic nanoparticles due to the ease of oxidation of both Fe and Zn [37]. The presence of Ni is attributed to the grid, C is from the PVP used to stabilize the nanoparticles while the other elements could simply be impurities emanating from various sources including the EDX detector [47].

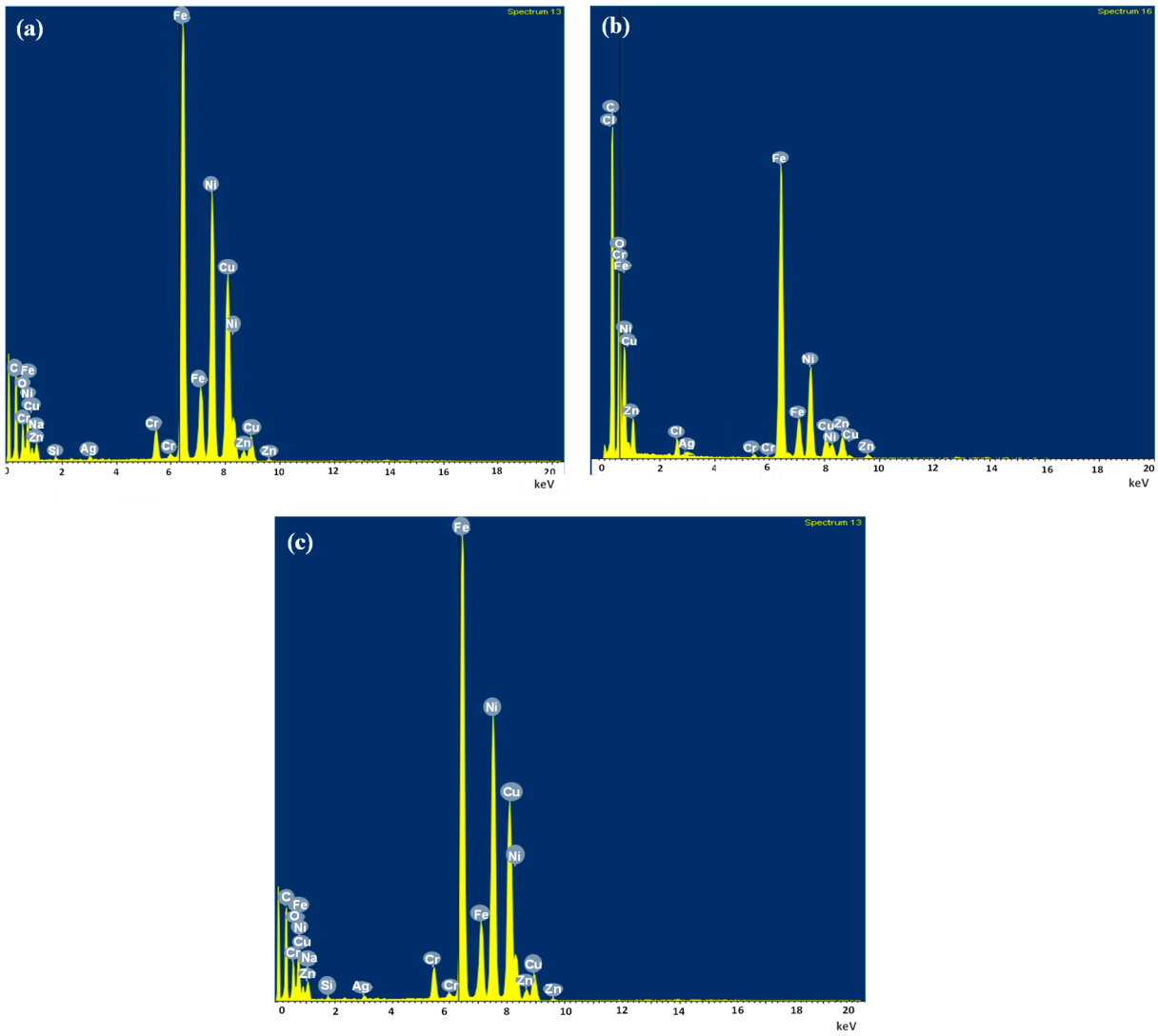

Figure 3. Energy-dispersive X-ray analysis of the trimetallic nanoparticles: (a) Fe/(Zn/Ag) 5(5:0.1), (b) Fe/Zn/Ag 5:5:0.1 and (c) Fe/Ag/Zn 5:0.1:5.

A further analysis of the trimetallic nanoparticles was carried out using XPS technique, which is a surface sensitive technique used for elemental identification within the surface of a material. The wide-scan survey and high-resolution spectral analyses were conducted; the high-resolution scan was used for the detailed chemical analysis of the elements identified in the full survey spectra. In Figure 4, the survey spectra of all the trimetallic nanoparticles show the presence of Fe, Zn, O and C; however, the XPS analysis of the Fe/Zn/Ag trimetallic system also detected the presence of Ag. Ag was not observed in the Fe/Ag/Zn and Fe/(Zn/Ag) systems because it is present in small amounts, whilst the other two metals are present in large quantities likely obscuring the Ag. However, even

© 2025 by the author(s). Distributed under a Creative Commons CC BY license.

Preprints.org (www.preprints.org) | NOT PEER-REVIEWED | Posted: 4 November 2025 doi:10.20944/preprints202511.0036.v1

though Ag was not detected using XPS in the aforementioned trimetallic systems, it was detected using XRD and EDX techniques. The C and O emanate from PVP and oxidation of Zn and Fe, respectively. These results corroborate those obtained with EDX and XRD analyses. The atomic percentages of each element present in the nanoparticles are summarized in Table 1. All three trimetallic nanoparticles show a high atomic percentage of O and C which have been attributed to the presence of iron and zinc oxides and the PVP used as the surfactant, respectively. Despite the same amounts being employed in the ratios, the atomic percentage of Zn is significantly higher than that of Fe in all three systems. The amount of Ag in the Fe/Zn/Ag system is much lower than the amounts of Fe and Zn, which is compatible with the ratio used.

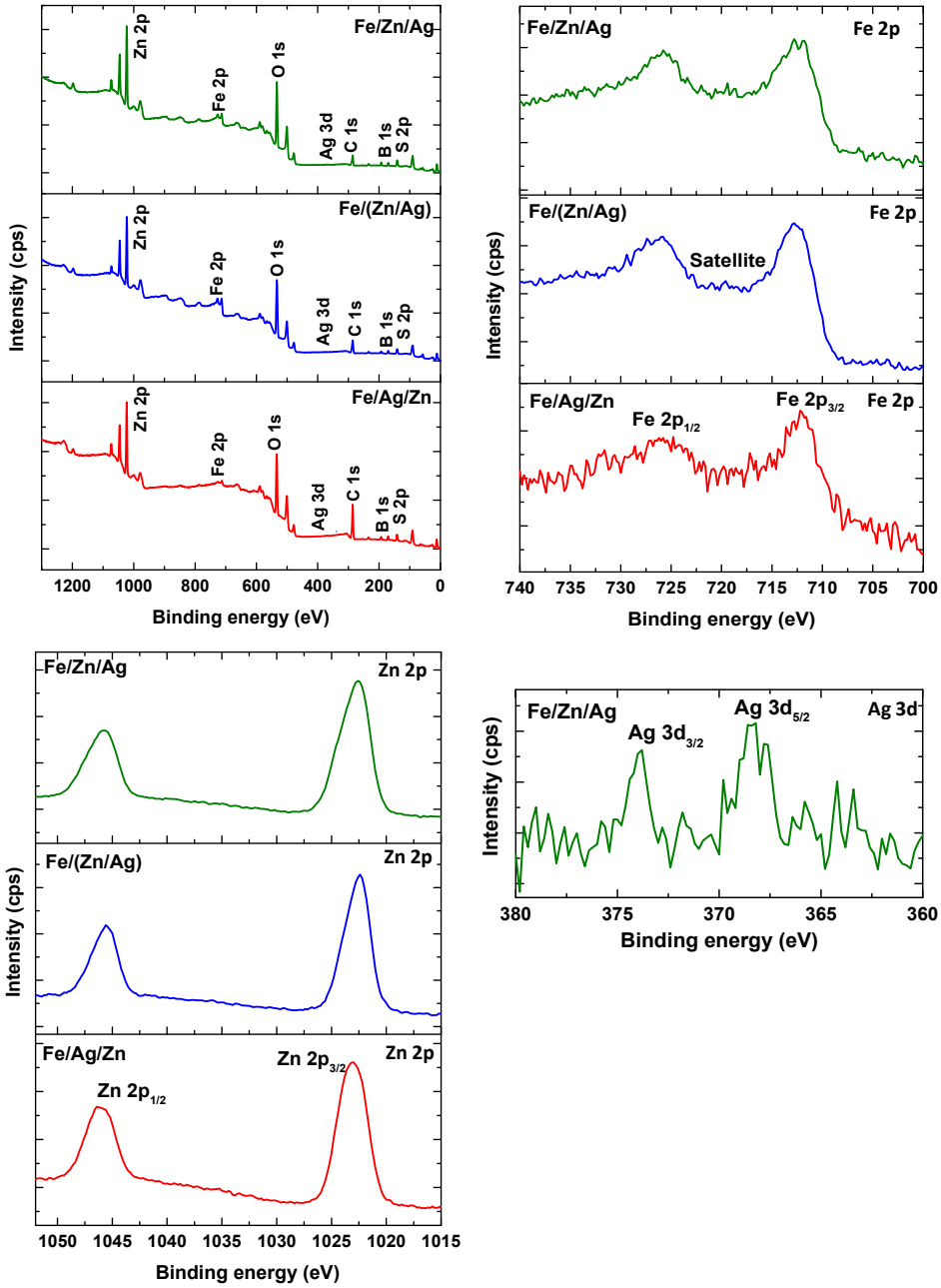

Figure 4. Survey spectra of the trimetallic nanoparticles: Fe/(Zn/Ag) 5(5:0.1), Fe/Zn/Ag 5:5:0.1 and Fe/Ag/Zn 5:0.1:5, their Fe 2p and Zn 2p high resolution spectra and Ag 3d high resolution spectrum of Fe/Zn/Ag 5:5:0.1 nanoparticles.

© 2025 by the author(s). Distributed under a Creative Commons CC BY license.

Preprints.org (www.preprints.org) | NOT PEER-REVIEWED | Posted: 4 November 2025 doi:10.20944/preprints202511.0036.v1

The Fe 2p high resolution spectra for all three trimetallic nanoparticles have two prominent photoelectron peaks at ~725 eV and ~712 eV which represent the binding energies of Fe $2p_{1/2}$ and Fe $2p_{3/2}$, respectively. The presence of ZVI is indicated by the aforementioned peaks, as well as a smaller band at a binding energy of ~706 eV [48]. The small peak at ~720 eV is a shake-up satellite which confirms the oxidation of Fe. The presence of a fraction of iron oxides and nZVI demonstrates that the nanoparticles have a core shell structure [48].

The XPS narrow spectra of Zn 2p shows two peaks at binding energies of ~1045 eV and ~1022 eV corresponding to the Zn $2p_{1/2}$ and Zn $2p_{3/2}$ of Zn^{2+}, respectively [49]. The difference in binding energy between these two peaks is about 23 eV, which is consistent with the zinc metal's published values [50]. Silver metal was detected only in the Fe/Zn/Ag trimetallic system and the Ag 3d XPS narrow spectrum is also displayed in Figure 4. The presence of pure silver is indicated by peaks at binding energies of 368.4 eV and 374.0 eV corresponding to Ag $3d_{5/2}$ and Ag $3d_{3/2}$, respectively.

Table 1. Atomic compositions of the trimetallic nanoparticles calculated from XPS spectra.

Sample	Element	Peak binding energy (eV)	Atomic %
Fe/Zn/Ag	C 1s	286.0	19.7
	O 1s	533.0	48.7
	Fe 2p	712.4	2.5
	Zn 2p	1022.9	14.0
	Ag 3d	368.8	0.1
Fe/(Zn/Ag)	C 1s	286.0	25.6
	O 1s	532.9	45.4
	Fe 2p	713.4	6.8
	Zn 2p	1022.8	10.9
Fe/Ag/Zn	C 1s	285.9	43.2
	O 1s	533.4	33.3
	Fe 2p	712.9	2.3
	Zn 2p	1023.0	9.0

The surface morphological properties of the products were conducted through the use of SEM and the resulting images are displayed in Figure 5a, Figure 5b and Figure 5c for Fe/(Zn/Ag), Fe/Ag/Zn and Fe/Zn/Ag, respectively. An assembly of well-defined 2D plate-like trimetallic nanoparticles are observed for Fe/(Zn/Ag) and Fe/Zn/Ag. The well-defined plate-like form was not maintained for the Fe/Ag/Zn trimetallic nanoparticles as an assembly of mixed morphologies consisting of predominantly plate-like and lesser botryoidal texture was observed. The disparity in morphological structures between Fe/Ag/Zn and other trimetallic nanoparticles is attributed to the particle agglomeration and smaller particle size. The structures and sizes of the nanostructures rely heavily on the synthesis method and experimental conditions. In this case, it is clearly observed that the different metal addition sequences (Fe/Ag/Zn, Fe/Zn/Ag and Fe/(Zn/Ag) influence the morphological properties of the nanostructures.

© 2025 by the author(s). Distributed under a Creative Commons CC BY license.

Preprints.org (www.preprints.org) | NOT PEER-REVIEWED | Posted: 4 November 2025 doi:10.20944/preprints202511.0036.v1

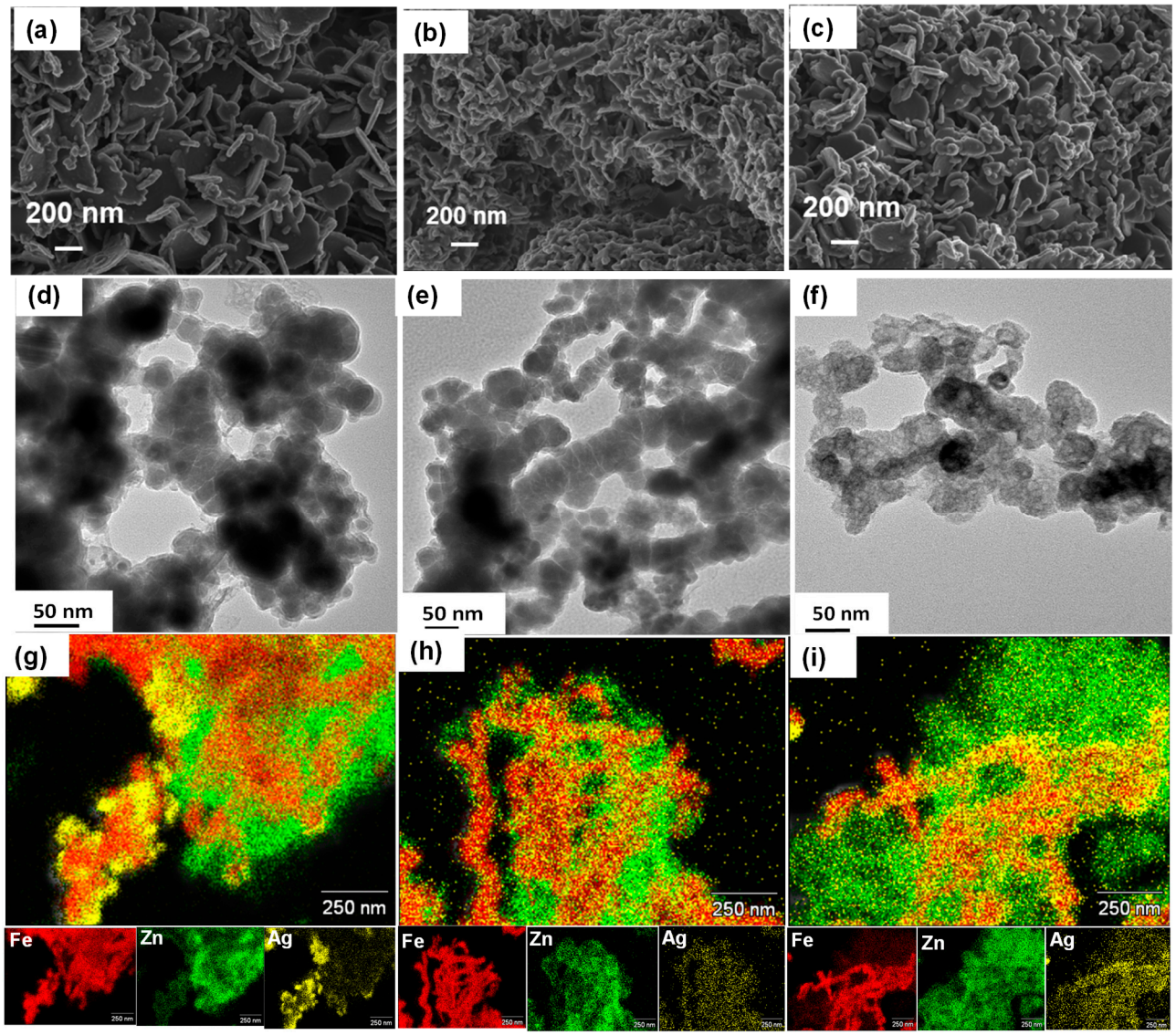

Figure 5. SEM images of (a) Fe/(Zn/Ag), (b) Fe/Ag/Zn and (c) Fe/Zn/Ag, TEM images of (d) Fe/(Zn/Ag), (e) Fe/Ag/Zn and (f) Fe/Zn/Ag, and elemental maps of (g) Fe/(Zn/Ag), (h) Fe/Ag/Zn and (i) Fe/Zn/Ag.

Furthermore, transmission electron microscopy (TEM) was used for the characterization of the nanoparticles in order to achieve high accuracy of the real particle size and shape [51]. The TEM images for the trimetallic nanoparticles are presented in Figure 5d, Figure 5e and Figure 5f. The complex structures of trimetallic nanoparticles constitute a mixture of core-shell structures and alloyed/intermediate structures [52,53]. The images show a morphology that is quasi-spherical and particles arranged in chain-like aggregates due to the magnetic dipole-dipole interactions between the particles and thus creating an arrangement of magnetic clusters [41]. This kind of structure has been reported in most studies involving nZVI and nZVI-based bimetallic nanoparticles [20,39,54,55]. Moreover, the trimetallic nanoparticles in Figure 5d and Figure 5e show a core-shell formation that reflects the oxidized part that surrounds the nZVI together with the other metals (Ag and Zn) [56]. The core-shell structure of nZVI nanoparticles has been reported before with the use of the $NaBH_4$ chemical reduction method for nanoparticle synthesis [57,58]. Furthermore, the core-shell structure is produced as a result of successive reduction of the nanoparticles involving the deposition of a secondary and/or tertiary metal on the surface of nZVI [53]. The pre-synthesized nZVI is chemically surrounded by the deposited metal/s [53]; in this case, both the metals and the oxides. The TEM results are congruous with the XRD results, revealing the crystalline structures of the nanoparticles notwithstanding the agglomeration. The Fe/Zn/Ag (Figure 5f) image has more irregular shaped

© 2025 by the author(s). Distributed under a Creative Commons CC BY license.

Preprints.org (www.preprints.org) | NOT PEER-REVIEWED | Posted: 4 November 2025 doi:10.20944/preprints202511.0036.v1

agglomerates that differ from the other images. The Zn or ZnO nanoparticles are supposedly attached to the ends of polymer chains with micelles on the inside [59]. Thus, in addition, the irregular agglomerates could be due to the formation of unique polymer-surfactant complexes and free micelles [59]. It can also be observed from the XRD pattern of the Fe/Zn/Ag trimetallic system that some of the peaks are not as sharp as the other trimetallic nanoparticles' peaks showing a more amorphous structure [60]. This, therefore, shows that the crystalline structure of the Fe/Zn/Ag trimetallic system is not as good as those of the other trimetallic systems [61,62].

Moreover, to verify the existence and distribution of Fe, Zn and Ag on the three samples, the EDS elemental maps were acquired and are shown in Figure 5g, Figure 5h and Figure 5i for Fe/(Zn/Ag), Fe/Ag/Zn and Fe/Zn/Ag, respectively. The elemental maps revealed the distribution and presence of Fe, Zn and Ag, elements, respectively. In all EDS mappings, the distinctive chain-like structure of the Fe is prominently evident, contrasting with the uneven distribution of the Zn and Ag in the images. However, in Figure 5h depicting the Fe/Ag/Zn nanoparticles, a more pronounced morphology is evident, and the distribution of Zn and Ag on the surface of nZVI exhibits a greater degree of uniformity.

Particle sizes of the nanoparticles were determined using image J. The particle size histograms of all the nanoparticles are shown in the appendix, Figure A1. The estimated average particle sizes of the Fe/Ag/Zn, Fe/Zn/Ag and Fe/(Zn/Ag) are 37, 35 and 45 nm, respectively. These are higher than the sizes obtained by XRD. This could be because XRD generally determines the crystallite size of which one particle can have many crystallites [63]; its more advantageous in cases where the particles are highly agglomerated [64]. These results are consistent with what other researchers have reported when comparing TEM and XRD particle sizes where the XRD size is normally smaller or equal to the TEM size [65].

3.2. Effect of Metal Addition Sequence on Methyl Orange Degradation

The results of the degradation profiles of MO using the three trimetallic nanoparticles are presented in Figure 6. The figure presents the rapid degradation of MO (pH ~4.5) using the Fe/Ag/Zn as compared to the slow degradation using the other trimetallic systems. It can be noted that the Fe/Ag/Zn nanoparticles degraded 100% of MO dye within 5 min into the reaction. This great reactivity of the Fe/Ag/Zn trimetallic nanoparticles could be a result of their smaller crystallite size compared to the other trimetallic systems. It has been established that smaller crystallite/nanoparticle sizes lead to an enhanced reactivity [66,67]. Bransfield et al. [68] and Yuan et al. [31] have demonstrated that the reactivity of the trimetallic system increases if the metals added onto the surface of iron have an increasing standard reduction potential (E^o) trend. For example, in the trimetallic system Fe/Cu/Ag prepared by Yuan et al. [31] the order of metal plating was as follows: Ag/Ag^+ (E^o= 0.7996 V) > Cu/Cu^{2+} (E^o= 0.3419 V) > Fe/Fe^{2+} (E^o= -0.447 V). Thus, in this case, the high activity of Fe/Ag/Zn could be attributed to the fact that both Fe and Zn are strong reducing agents and are capable of releasing electrons that are required to generate atomic hydrogen that facilitates the reaction in the presence of water or dissolved oxygen [69,70]. The bimetallic Fe/Zn and Fe/Ag systems were also studied, and the results are presented in Figure A2. These bimetallic systems show an overall good performance as compared to the Fe/Zn/Ag and Fe/(Zn/Ag) trimetallic systems. However, the Fe/Ag/Zn system still had the highest degradation efficiency as compared to the bimetallic systems. Moreover, in a trimetallic system, the reactivity is thought to be more influenced by the second metal on the surface of iron (Zn in the Fe/Ag/Zn system) than the first one (Ag) [71]. This is despite the exceptions of either the obscuring of the first metal deposited onto nZVI by the second metal or by the deposition of the second metal on some non-accessible reactive sites by MO at the surface of nZVI particles [71].

© 2025 by the author(s). Distributed under a Creative Commons CC BY license.

Preprints.org (www.preprints.org) | NOT PEER-REVIEWED | Posted: 4 November 2025 doi:10.20944/preprints202511.0036.v1

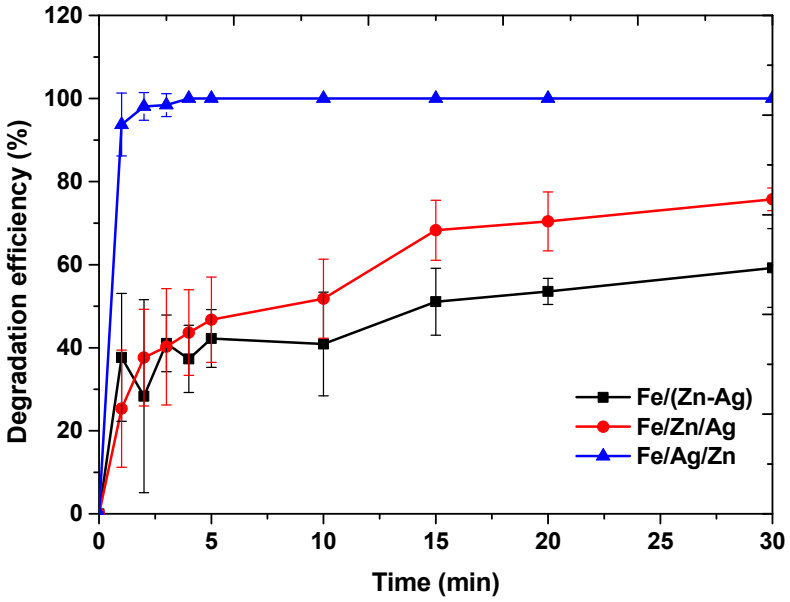

Figure 6. Degradation efficiencies of 10 mg/L methyl orange dye using 10 mg of the trimetallic nanoparticles (Fe/Zn/Ag 5:5:0.1, Fe/Ag/Zn 5:0.1:5 and Fe/(Zn/Ag) 5:(5:0.1)).

The kinetic data of the degradation of MO dye using the trimetallic nanoparticles was fitted in three models, the zeroth-, first- and second-order models and the plots are presented in Figure 7. As observed, the slope of the Fe/Ag/Zn plot in all kinetic models steepened, thereby signifying that the k_0, k_1 and k_2 of the zeroth-, first and second-order models, respectively, were higher than those of the other trimetallic systems. The R^2 values of the three kinetic models are summarized in Table 3. It can be observed from the table that the second-order kinetic model best described the degradation of MO dye and the R^2 values were above 0.80. Thus, the second order rate constants for the reaction of the nanoparticles with MO were as follows: Fe/Ag/Zn (0.0744 $(mg/L)^{-1}min^{-1}$) > Fe/Zn/Ag (0.0050 $(mg/L)^{-1}min^{-1}$) > Fe/(Zn/Ag) (0.0025 $(mg/L)^{-1}min^{-1}$). The reactivity of the Fe/Ag/Zn trimetallic system was found to be 15 times higher than that of Fe/Zn/Ag and 30 times higher than that of Fe/(Zn/Ag) trimetallic system. The reactivity of the Fe/Zn/Ag system was 2 times higher than that of the Fe/(Zn/Ag) trimetallic system. This observation suggests that the order of metal addition in the trimetallic system has greatly influenced the reactivity of the trimetallic system. Most studies involving the degradation of pollutants using nZVI and nZVI-based bimetallic and trimetallic nanoparticles fitted the degradation on the pseudo-first order kinetic model [31,38,72–74]. However, there are studies showing a second order fit for degradation of pollutants by nZVI and iron oxide nanoparticles [75,76]. In these studies, the second order kinetic fit was mainly attributed to the large access of reducing agent, which promotes the corrosion of iron [75]. These results show that the rate of the reaction is proportional to the square of the concentration of the dye [77]. Moreover, Table 2 shows a comparison of the dye removal efficiencies obtained in previous studies to the one obtained in this study using Fe/Ag/Zn trimetallic nanoparticles. In comparison with previous studies, the Fe/Ag/Zn system reported in this work showed a better catalytic activity and behaved similarly to the Fe/Cu/Ag system [32]. Moreover, the Fe/Ag/Zn system was able to degrade 100% of the dye within 1 min into the reaction at a lower nanoparticle dosage, pH and dye concentration than in the other studies. Furthermore, despite the lower dye concentration in this study, the results show that the Fe/Ag/Zn system performed better than some previous studies with supported nanoparticles at a relatively lower nanoparticle dose. This, therefore, shows that dye degradation in this study was more rapid and efficient than in the reported previous studies.

© 2025 by the author(s). Distributed under a Creative Commons CC BY license.

Preprints.org (www.preprints.org) | NOT PEER-REVIEWED | Posted: 4 November 2025 doi:10.20944/preprints202511.0036.v1

Table 2. Reported dye removal percentages by nZVI, bimetallic and trimetallic nZVI nanoparticles in comparison with the current study.

	NP used	Dosage (mg/L)	pH	Temperature (°C)	Dye concentration (mg/L)	Removal %	Reaction time (min)	References
1	nZVI	150	7.0	Room temperature	MO-40	98	30	[78]
2	B nZVI	500	6.5	30	MO-100	79.5	10	[79]
3	B* nZVI	600	4.1	Room temperature	MO-300	98.5	10	[80]
4	B Fe/Pd	500	6.2	25	MO-200	91.9	20	[25]
5	Fe/Ni	3000	-	28±2	Orange G-150	99.9	10	[81]
6	Fe/Cu/Ag	200	3.0	Room temperature	MO-10	100.0	1	[32]
7	Fe/Ag/Zn	200	3.0	Room temperature	MO-10	100.0	1	Current study

[B] Bentonite supported, [B*] Biochar supported.

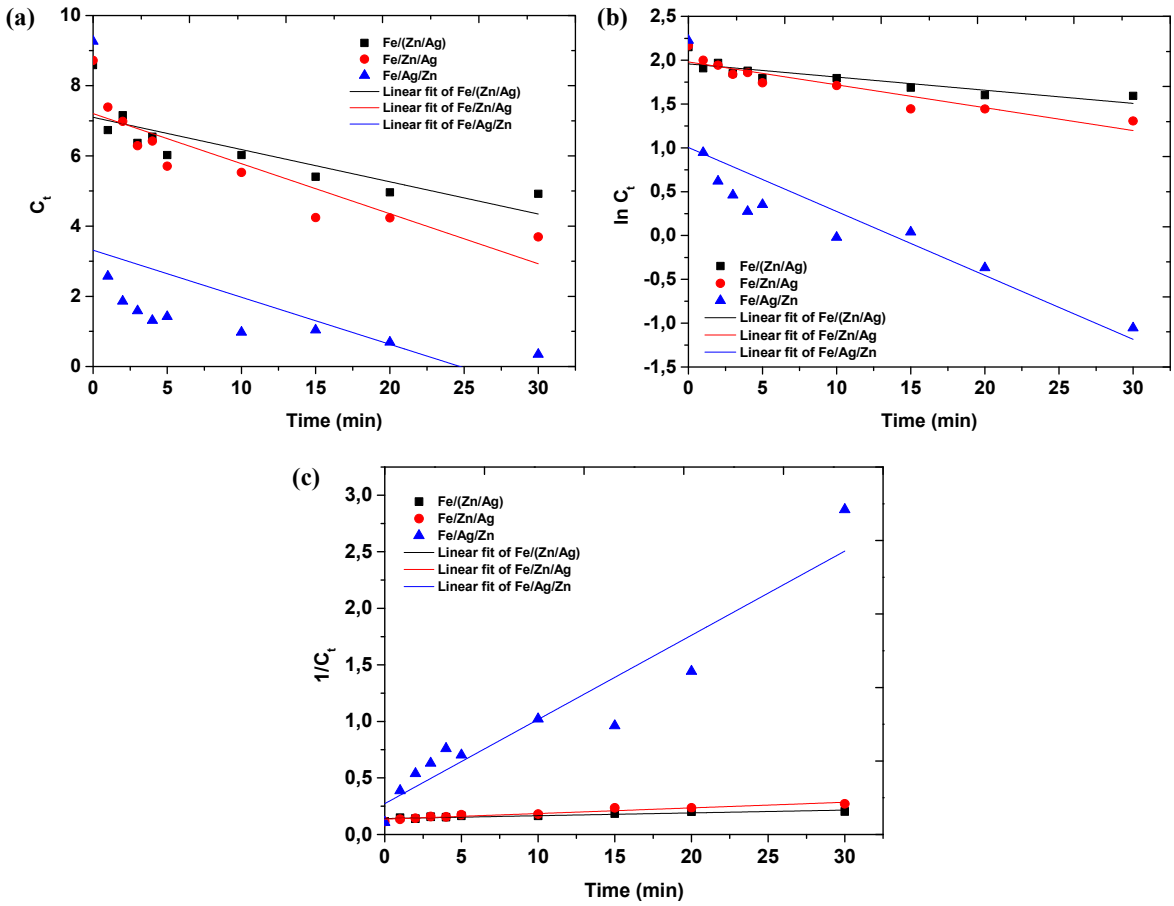

Figure 7. Kinetic plots of the synthesized nanoparticles: (a) zeroth-order, (b) first-order and (c) second-order.

However, the reactivity of nZVI-based trimetallic nanoparticles and mechanism has not been clearly stated and remains incomprehensible and controversial [31]. There are previously

© 2025 by the author(s). Distributed under a Creative Commons CC BY license.

Preprints.org (www.preprints.org) | NOT PEER-REVIEWED | Posted: 4 November 2025 doi:10.20944/preprints202511.0036.v1

hypothesized mechanisms of the reaction of trimetallic nanoparticles in the degradation of organic pollutants. The degradation process has been said to either proceed by the adsorption of atomic hydrogen onto the transition metal additive [82] and/or that the transition metal may produce atomic hydrogen that is surface-bound [68,83]. In addition, the surface additives could boost the reactivity by increasing the iron corrosion rate by forming galvanic couples due to the potential difference between nZVI and additives [68].

Table 3. R^2 values of the zeroth-, first- and second-order kinetic data of the trimetallic nanoparticles.

	R^2 values		
	Zeroth-order	**First-order**	**Second-order**
Fe/(Zn/Ag)	0.6363	07229	0.8052
Fe/Zn/Ag	0.7655	0.8578	0.9506
Fe/Ag/Zn	0.1662	0.6537	0.9107

3.3. Evaluating the Catalytic Activity of the Trimetallic Systems

The number of active sites of the trimetallic nanoparticles was used to establish the sites on which the reaction occurs [84]. These were equated to the number of moles of the metal ions in a specific quantity of catalyst for a certain reaction [84], 10 mg catalyst loading in this case. The results of the active sites, TON and TOF calculations are summarized in Table 4. The number of active sites for all three trimetallic nanoparticles is the same because the ratios of the metals used in each system are the same. However, the TON and TOF values decreased in this trend: Fe/Ag/Zn > Fe/Zn/Ag > Fe/(Zn/Ag). This trend is similar to that of the degradation and reaction kinetics results reported above. Although the number of active sites of the nanoparticles is the same, their catalytic efficiencies differ. This could be attributable to that in the Fe/(Zn/Ag) and Fe/Zn/Ag systems, the active sites are possibly ineffective and may not be directly involved in the catalytic reaction [85]. Catalytic active sites are said to be responsible for the reactivity of the catalyst; thus the inaccessibility of the active sites leads to a decline in catalytic activity [86]. Furthermore, the Fe/Ag/Zn particles on the TEM images are far less agglomerated than the Fe/Zn/Ag particles. It has been established that surface sites of dispersed nanoparticles are more accessible than surface sites of agglomerated nanoparticles [87]; which could be attributable to the Fe/Ag/Zn system showing the highest TOF value. The TOF value of the Fe/Ag/Zn, which is the best-performing catalyst, was 0.7461 min^{-1}, meaning that 0.7461 moles of dye was converted by one active site per minute.

Table 4. The number of active sites, TON and TOF values of the trimetallic nanoparticles calculated at 5 min reaction time.

	Degradation efficiency (%)	**Number of active sites (moles)**	**TON**	**TOF (min^{-1})**
Fe/(Zn/Ag)	42.21	4.09×10^{-5}	1.5669	0.3134
Fe/Zn/Ag	46.73	4.09×10^{-5}	1.7534	0.3507
Fe/Ag/Zn	100.00	4.09×10^{-5}	3.7307	0.7461

3.4. Effect of Reaction Conditions on Catalyst Performance

The effect of operational parameters on the degradation of MO dye in aqueous solution using the Fe/Ag/Zn trimetallic nanoparticles was investigated. The Fe/Ag/Zn trimetallic system was used due to its excellent reactivity for MO degradation compared with the other trimetallic systems prepared in this study. The catalytic decolourization and degradation of MO dye using the trimetallic nanoparticles was carried out using the second-order kinetic model.

© 2025 by the author(s). Distributed under a Creative Commons CC BY license.

Preprints.org (www.preprints.org) | NOT PEER-REVIEWED | Posted: 4 November 2025 doi:10.20944/preprints202511.0036.v1

3.4.1. Effect of Initial Solution pH

The pH of the solution plays a significant role in the degradation process of different organic pollutants and thus it was of interest to study its effect on MO degradation using Fe/Ag/Zn 5:0.1:5 trimetallic nanoparticles [88–90]. The effect of pH on the degradation of MO was studied in the pH range 3-12 and the degradation results are shown in Figure 7a. Solution pH was adjusted prior to degradation tests. Figure 8a shows that the degradation efficiency of MO decreases with an increase in solution pH. At lower pH values (pH 3 and 6), the degradation efficiency of MO occurs rapidly and reaches 100% within 5 min. When the pH of the solution was increased to 9 and 12, the degradation efficiencies of MO drastically decreased. The enhancement in degradation efficiency of MO at low pH could be attributed to the high concentration of hydrogen ions which are actively involved in nZVI reductive reaction [91]. At high pH values, the decline in degradation efficiency is primarily due to the development of ferrous/ferric hydroxide complexes made from Fe (III), Fe (II) and OH^- ions; resulting in the deactivation of the nZVI catalyst [92]. The second-order degradation rate constants are shown in Figure 8b. It can be observed that the rate constants decrease with an increase in pH values, 0.3917, 0.1393, 0.0217 and 0.0047 $(mg/L)^{-1}min^{-1}$ at pH 3, 6, 9 and 12, respectively. The second-order rate constant at the pH of 3 was 83 times higher than that at pH 12 and 18 times higher than that at pH 9. Thus, the highest reaction rate of degradation is obtained at lower pH and these results are similar to what other researchers have previously reported [80,93]. Therefore, it can be inferred that acidic conditions are best suited for the degradation of MO by Fe/Ag/Zn trimetallic nanoparticles.

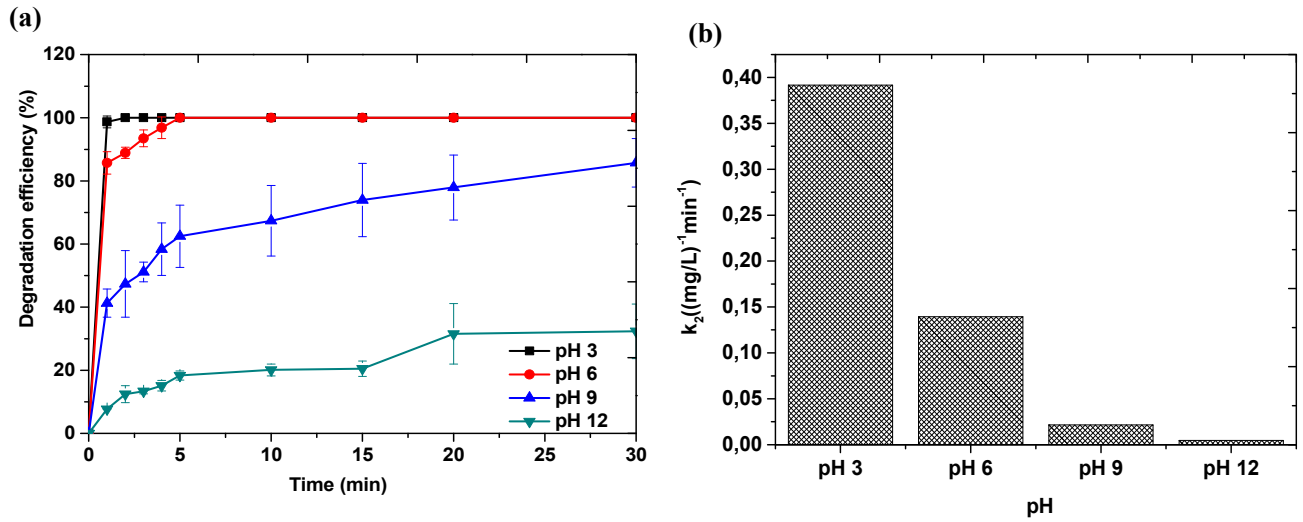

Figure 8. The degradation efficiencies of 10 mg/L methyl orange dye using 10 mg Fe/Ag/Zn 5:0.1:5 nanoparticles at different pH values (a) and the second-order rate constants at different pH values (b).

3.4.2. Effect of Initial Methyl Orange Dye Concentration

The influence of initial MO dye concentration of the degradation efficiency by Fe/Ag/Zn system is shown in Figure 9a. The plot shows that the degradation efficiency of MO decreases with an increase in initial MO concentration. However, the lower initial concentrations (10, 30 and 50 mg/L) reached 100% degradation within 15 min into the reaction, though degradation occurs more rapidly at the initial MO concentration of 10 mg/L where 100% degradation is obtained within 2 min. When the initial concentration was increased to 150 and 300 mg/L, the degradation efficiency decreased. Furthermore, the results for the rate of reaction of MO degradation at different initial concentration are summarised in Figure 9b on the plot of k_2 versus initial dye concentration. The second-order rate constants were 2.6069, 0.0799, 0.0141, 0.0020 and 2.296×10^{-4} $(mg/L)^{-1}min^{-1}$ for 10, 30, 50, 150 and 300 mg/L, respectively. The second-order rate constants of MO degradation by the Fe/Ag/Zn

© 2025 by the author(s). Distributed under a Creative Commons CC BY license.

Preprints.org (www.preprints.org) | NOT PEER-REVIEWED | Posted: 4 November 2025 doi:10.20944/preprints202511.0036.v1

nanoparticles decreased drastically with an increase in the initial dye concentration. The rate constant at the initial dye concentration of 10 mg/L was 33 times higher than that at 25 mg/L, 185 times higher than that at 50 mg/L, 1291 times higher than that at 150 mg/L and 11351 times higher than that at 300 mg/L. This shows that at lower dye concentrations; the rate of the reaction is extremely fast. Similar observations of decreasing degradation efficiencies with increasing initial pollutant concentration have been previously reported [94,95]. This trend can be attributed to the rapid occupation of all the trimetallic nanoparticles active sites by MO molecules at high dye concentration [95]. Furthermore, the particles' adsorption capacity is limited and the increase in MO concentration leads to a competitive adsorption between MO molecules whereby the adsorbed molecules will impede the adsorption and reduction of other molecules in the solution [37,94].

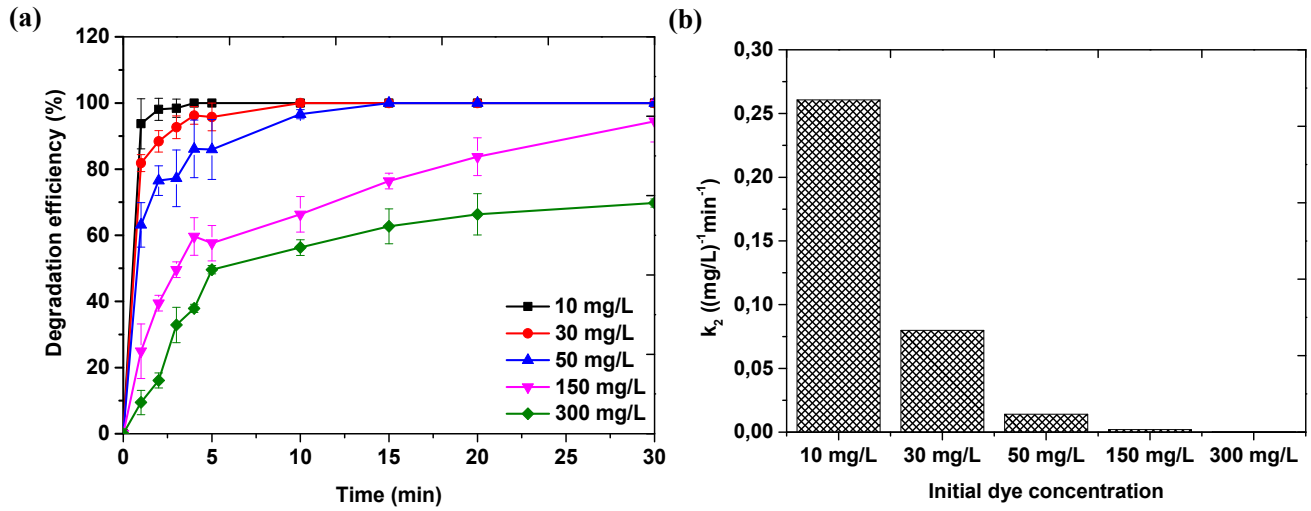

Figure 9. The degradation efficiencies of 10 mg/L methyl orange dye using 10 mg Fe/Ag/Zn 5:0.1:5 nanoparticles at different initial dye concentrations (a) and the apparent rate constants at different methyl orange dye concentrations (b).

3.4.3. Effect of Initial Nanoparticle Dosage

The effect of Fe/Ag/Zn trimetallic nanoparticle loading on the degradation of MO was studied with three different catalyst loadings (4, 7 and 10 mg). As depicted in Figure 10a, the degradation efficiency of MO increases with increasing nanoparticle dosage. The lowest loadings of 4 and 7 mg do not reach 100% degradation within the set reaction time of 30 min. On the contrary, the 10 mg nanoparticle loading reached 100% degradation within 2 min reaction. Moreover, the second-order rate constants increase with an increase in nanoparticle dosage as shown in Figure 10b. The degradation rate constants are 0.0212, 0.0343 and 2.6069 $mg/L^{-1}min^{-1}$ for 4, 7 and 10 mg nanoparticle loadings, respectively. The k_2 at the initial nanoparticle dosage of 10 mg was 76 times higher than that at 7 mg and 123 times higher than that at 4 mg dosage. These observations may be ascribed to the fact that at a high nanoparticle dosage there are more particles that can provide more active surface sites for collision with MO dye molecules to achieve greater dye removal efficiency [91,96]. This was an expected observation as the same was found to be the case in previous studies involving degradation of organic pollutants by nZVI and nZVI-based particles [79,91].

© 2025 by the author(s). Distributed under a Creative Commons CC BY license.

Preprints.org (www.preprints.org) | NOT PEER-REVIEWED | Posted: 4 November 2025 doi:10.20944/preprints202511.0036.v1

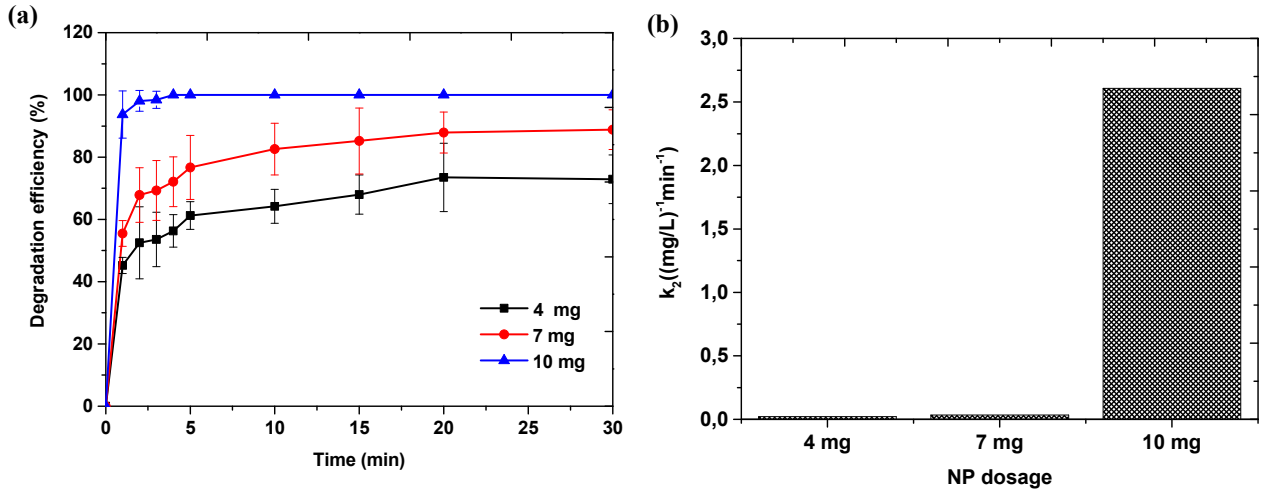

Figure 10. The degradation efficiencies of 10 mg/L methyl orange dye using Fe/Ag/Zn 5:0.1:5 nanoparticles at different initial nanoparticle dosages (a) and the apparent rate constants at different initial nanoparticle dosages (b).

3.5. Methyl Orange Degradation Products and Pathway

The degradation pathway and products from MO degradation using Fe/Ag/Zn 5:0.1:5 trimetallic nanoparticles were determined using LC-MS analysis. The total mass chromatograms of MO and its degradation products at 0, 1 and 30 min of degradation are shown in Figure 11. According to the results obtained by UV-vis analysis, the degradation of MO occurs within 1 min. Similarly, from the LC-MS results, it can be seen that the peak for MO eluted at 2.02 min retention time on the chromatogram completely disappears within 1 min (Figure A3, Appendix). The mass spectrogram in Figure 11a at 0 min has an identified peak at m/z value of 306 corresponding to MO dye before degradation. Figure 11b shows the mass spectrogram at 1 min which shows peaks at m/z values of 122, 157 and 171 which were identified as N,N dimethyl benzeneamine, benzenesulfonic acid and sulfanilic acid, respectively. These were due to the symmetrical cleavage of the azo-bond on the MO structure. In this case, the degradation occurred rapidly compared to some previous studies involving the degradation of MO dye [97–99]. Generally, before the appearance of peaks at m/z 157 and 121, the total mass spectrogram from MO degradation shows peaks at m/z 172 and 136 which are directly due to the cleavage of the azo-bond [98,99].

Moreover, Figure 11c and Figure 11d show the total mass chromatograms at 30 min at retention times of 5.51 and 5.00 min, respectively. Figure 11c has a peak at m/z 157 and Figure 10d has a peak at m/z 122 which were both identified above as products from MO degradation. However, these products have both reduced in intensity proving their disappearance as degradation duration increases. Thus, with an increase in reaction time and introduction of other parameters favouring mineralization, there is a possibility of formation of CO_2 and H_2O as the products from MO degradation are more prone to mineralization than MO itself [100–102]. The peak at m/z 256 on Figure 11c could not be identified as it does not correspond to masses of the products from MO degradation or the nanoparticles used in the study. Thus, it could potentially be due to impurity ions that can enter the mass analyser through the column, the sample itself or mobile phase solvents providing peaks with high intensities on the total ion chromatogram [103]. Using the above information, a degradation pathway was identified as shown in Figure 12. The degradation starts with the cleavage of the azo-bond producing sulfanilic acid and N,N dimethyl-p-phenyldiamine which further degrade and possibly lead to mineralization.

© 2025 by the author(s). Distributed under a Creative Commons CC BY license.

Preprints.org (www.preprints.org) | NOT PEER-REVIEWED | Posted: 4 November 2025 doi:10.20944/preprints202511.0036.v1

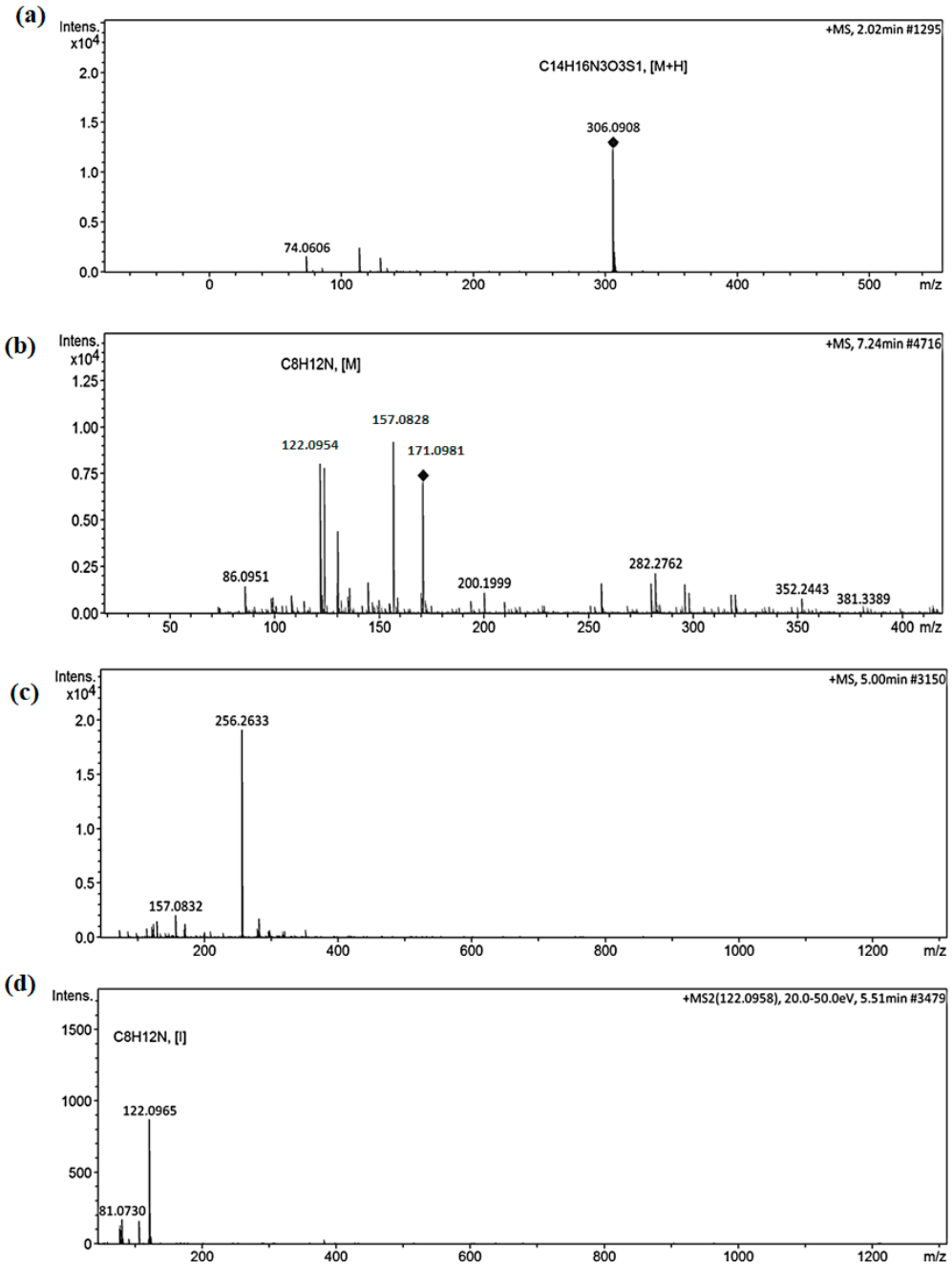

Figure 11. Total ion chromatograms of methyl orange degradation at (a) 0 min, (b) 1 min, (c) 30 min at retention time of 5.51 min and (d) 30 min at retention time of 5.00 min.

© 2025 by the author(s). Distributed under a Creative Commons CC BY license.

Preprints.org (www.preprints.org) | NOT PEER-REVIEWED | Posted: 4 November 2025 doi:10.20944/preprints202511.0036.v1

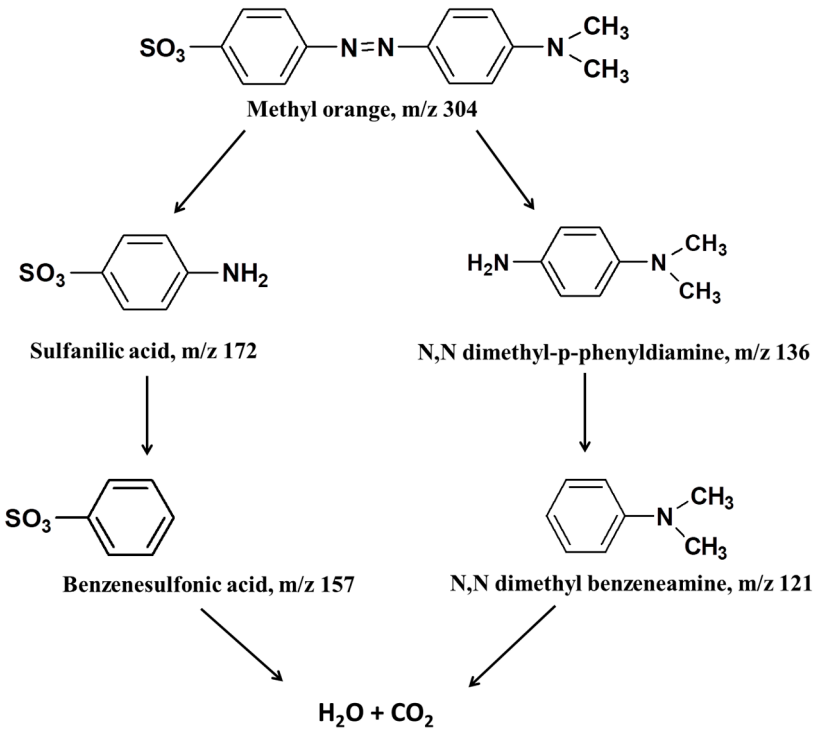

Figure 12. Possible degradation pathway of methyl orange using Fe/Ag/Zn nanoparticles.

3.6. Probable Methyl Orange Degradation Mechanism by Fe/Ag/Zn Trimetallic Nanoparticles

The mechanism for degradation or removal of organic pollutants by trimetallic nanoparticles has not been identified and is deemed controversial [71]. However, herein, an explanation for a hypothetical possible degradation mechanism for the MO dye by trimetallic nanoparticles was attempted. Studies have shown that the degradation of dyes by nZVI is a redox reaction and can occur in two ways: oxidation in the presence of dissolved oxygen and reduction in anaerobic conditions [104,105]. The Fe/Ag/Zn system contains two reducing agents (Fe and Zn); which are both strong reducing agents [105,106]. Since the experiments were done in an open-batch system, before the invasion of oxygen into the mixture, the following reactions can take place:

$$Fe^0 + 2H_2O \rightarrow Fe^{2+} + H_2 + 2OH^- \quad (12)$$

$$Fe^0 + 2H^+ \rightarrow Fe^{2+} + H_2 \quad (13)$$

$$Zn^0 + 2H_2O \rightarrow Zn^{2+} + H_2 + 2OH^- \quad (14)$$

Equations (12-14) show the corrosion of Fe^0 and Zn^0 in the presence of water and H^+. In this case there are various potential reducing agents for the MO dye in the system (Fe^0, Zn^0, Fe^{2+}, Zn^{2+} and H_2) [105]. As the reaction continues in the presence of dissolved oxygen, the corrosion of Fe^0 can happen as follows:

$$Fe^0 + O_2 + 2H^+ \rightarrow Fe^{2+} + H_2O_2 \quad (15)$$

$$Fe^0 + H_2O_2 + 2H^+ \rightarrow Fe^{2+} + 2H_2O \quad (16)$$

$$Fe^{2+} + H_2O_2 \rightarrow Fe^{3+} + \bullet OH + OH^- \quad (17)$$

Equations (15-17) explain the oxidation of iron in the presence of dissolved oxygen to produce H_2O_2 which further reacts with water to produce hydroxyl radicals (•OH) [107]. The •OH then acts as an oxidizing agent for the MO dye or its products. Lastly, the purpose of the Ag in the nanoparticles was to form Ag-H structure after the corrosion of Fe and/or Zn in aqueous solution; the

© 2025 by the author(s). Distributed under a Creative Commons CC BY license.

Preprints.org (www.preprints.org) | NOT PEER-REVIEWED | Posted: 4 November 2025 doi:10.20944/preprints202511.0036.v1

Ag-H structure also has a potential to act as a reducing agent that can cleave the azo-bond of the MO structure [108].

Thus, in summary, the first step in the degradation of the MO would be the cleavage of the azo-bond as a result of reduction by the reducing agents described above. Thereafter, aromatic amines are produced with further protonation from water, which is a proton donor and electrons released from corrosion [109,110]. Finally, with the introduction of the dissolved oxygen in the system, the •OH radicals will lead to mineralization of the products. Thus, the degradation of MO using Fe/Ag/Zn probably occurs via a combination of processes.

4. Conclusions

In this study, three trimetallic nanoparticles (Fe/Ag/Zn, Fe/Zn/Ag and Fe/(Zn/Ag)) with different metal addition sequences were successfully synthesized, characterized and tested. The TEM, XRD, SEM and XPS analyses confirmed the successful synthesis of these nanoparticles with TEM and EDS mapping images showing chain-like structure of the particles due to magnetic interactions between them. The catalytic activity of the Fe/Ag/Zn was found to be higher than those of the other trimetallic systems with the TOF value of 0.7461 min^{-1}. This showed that the performance of the trimetallic nanoparticles was affected by the sequence of metal addition onto the surface of nZVI. The degradation efficiency of MO by the Fe/Ag/Zn 5:0.1:5 nanoparticles and the reactivity of the nanoparticles were shown to be greatly affected by the pH, initial MO dye concentration and nanoparticle dosage. The k_2 at pH 3 was 83 times higher than that at pH 12 and 18 times higher than that at pH 9. At the initial nanoparticle dosage of 10 mg the k_2 was 2.6069 $(mg/L)^{-1}min^{-1}$ which was 76 times higher than that as 7 mg and 123 times higher than that at 4 mg dosage. The k_2 at the initial dye concentration of 10 mg/L was multiple times higher than the ones at higher initial dyes concentrations. In general, the process was proven to be highly acid-driven. The results of LC-MS analysis show that MO degradation occurred within 1 min and products formed were prone to mineralization than the MO dye. Thus, the Fe/Ag/Zn trimetallic nanoparticles can be very effective at degrading textile wastewaters polluted with dyes such as MO.

Acknowledgments: The authors gratefully acknowledge Mintek for financial support. They would also like to thank the University of the Witwatersrand and the Department of Science and Innovation/Mintek Nanotechnology Innovation Centre for their support and facilities.

References

1. H. Yukseler, N. Uzal, E. Sahinkaya, M. Kitis, F.B. Dilek, U. Yetis, Analysis of the best available techniques for wastewaters from a denim manufacturing textile mill. J. Environ. Manage. 203 (2017) 1118–1125. https://doi.org/10.1016/j.jenvman.2017.03.041.
2. L. Aljerf, High-efficiency extraction of bromocresol purple dye and heavy metals as chromium from industrial effluent by adsorption onto a modified surface of zeolite: Kinetics and equilibrium study. J. Environ. Manage. 225 (2018) 120–132. https://doi.org/10.1016/j.jenvman.2018.07.048.
3. I.G. Laing, The impact of effluent regulations on the dyeing industry. Rev. Prog. Color. Relat. Top. 21 (1991) 56–71. https://doi.org/10.1111/j.1478-4408.1991.tb00081.x.
4. F. Gahr, F. Hermanutz, W. Oppermann, Ozonation-an important technique to comply with new German laws for textile wastewater treatment. Interciencia 30 (1994) 255–263. https://doi.org/10.2166/WST.1994.0115.
5. P.C. Vandevivere, R. Bianchi, W. Verstraete, Review treatment and reuse of wastewater from the textile wet-processing industry: review of emerging technologies. J. Chem. Technol. Biotechnol. 72 (1998) 289–302. https://doi.org/10.1002/chin.199843337.
6. D.A. Yaseen, M. Scholz, Textile dye wastewater characteristics and constituents of synthetic effluents : A critical review. Int. J. Environ. Sci. Technol. 16 (2019) 1193–1226. https://doi.org/10.1007/s13762-018-2130-z.

© 2025 by the author(s). Distributed under a Creative Commons CC BY license.

Preprints.org (www.preprints.org) | NOT PEER-REVIEWED | Posted: 4 November 2025 doi:10.20944/preprints202511.0036.v1

7. N.C. Cinperi, E. Ozturk, N.O. Yigit, M. Kitis, Treatment of woolen textile wastewater using membrane bioreactor, nanofiltration and reverse osmosis for reuse in production processes. J. Clean. Prod. 223 (2019) 837–848. https://doi.org/10. https://doi.org/10.1016/j.jclepro.2019.03.166.
8. M.R. Sarker, M. Chowdhury, A. Deb, Reduction of color intensity from textile dye wastewater using microorganisms: A review. Int. J. Curr. Microbiol. Appl. Sci. 8 (2019) 3407–3415. https://doi.org/10.20546/ijcmas.2019.802.397.
9. D. Mikucioniene, D.M. García, R. Repon, R. Mila, G. Priniotakis, Understanding and addressing the water footprint in the textile sector: A review. AUTEX Res. J. 24 (2024) 1–27. https://doi.org/10.1515/aut-2024-0004.
10. S. Popli, U.D. Patel, Destruction of azo dyes by anaerobic–aerobic sequential biological treatment: A review. Int. J. Environ. Sci. Technol. 12 (2015) 405–420. https://doi.org/10.1007/s13762-014-0499-x.
11. I.K. Konstantinou, T.A. Albanis, TiO_2-assisted photocatalytic degradation of azo dyes in aqueous solution: kinetic and mechanistic investigations: A review. Appl. Catal. B Environ. 49 (2004) 1–14. https://doi.org/10.1016/j.apcatb.2003.11.010.
12. K.-T. Chung, C.E. Cerniglia, Mutagenicity of azo dyes: Structure-activity relationships. Mutat. Res. 277 (1992) 201–220. https://doi.org/10.1016/0165-1110(92)90044-A.
13. P.A. Carneiro, G.A. Umbuzeiro, D.P. Oliveira, M.V.B. Zanoni, Assessment of water contamination caused by a mutagenic textile effluent/dyehouse effluent bearing disperse dyes. J. Hazard. Mater. 174 (2010) 694–699. https://doi.org/10.1016/j.jhazmat.2009.09.106
14. P.I.M. Firmino, M.E.R. da Silva, F.J. Cervantes, A.B. dos Santos, Colour removal of dyes from synthetic and real textile wastewaters in one- and two-stage anaerobic systems. Bioresour. Technol. 101 (2010) 7773–7779. https://doi.org/10.1016/j.biortech.2010.05.050.
15. D. Chandran, Review of the textile industries waste water treatment methodologies. Int. J. Sci. Eng. Res. 7 (2015) 392–403.
16. M. T. Moghadam, F. Qaderi, Modeling of petroleum wastewater treatment by Fe/Zn nanoparticles using the response surface methodology and enhancing the efficiency by scavenger. Results Phys. 15 (2019) 102566. https://doi.org/10.1016/j.rinp.2019.102566.
17. P.K. Boruah, B. Sharma, I. Karbhal, M. V. Shelke, M.R. Das, Ammonia-modified graphene sheets decorated with magnetic Fe_3O_4 nanoparticles for the photocatalytic and photo-Fenton degradation of phenolic compounds under sunlight irradiation. J. Hazard. Mater. 325 (2017) 90–100. https://doi.org/10.1016/j.jhazmat.2016.11.023.
18. Y. Liu, S. Zhou, F. Yang, H. Qin, Y. Kong, Degradation of phenol in industrial wastewater over the F-Fe/TiO_2 photocatalysts under visible light illumination. Chinese J. Chem. Eng. 24 (2016) 1712–1718. https://doi.org/10.1016/j.cjche.2016.05.024.
19. S.L. Alamo-nole, S. Bailon-Ruiz, T. Luna-Pineda, O. Perales-Perez, F.R. Roman, Photocatalytic activity of quantum dot–magnetite nanocomposites to degrade organic dyes in the aqueous phase. J. Mater. Chem. A 1 (2013) 5509–5516. https://doi.org/10.1039/c3ta01135f.
20. N. Rahman, Z. Abedin, M.A. Hossain, Rapid degradation of azo dyes using nano-scale zero valent iron. Am. J. Environ. Sci. 10 (2014) 157–163. https://doi.org/10.3844/ajessp.2014.157.163.
21. S. Huang, L. Gu, N. Zhu, K. Feng, H. Yuan, Z. Lou, Y. Li, A. Shan, Heavy metal recovery from electroplating wastewater by synthesis of mixed-Fe_3O_4@ SiO_2/metal oxide magnetite photocatalysts. Green Chem. 16 (2014) 2696–2705. https://doi.org/10.1039/c3gc42496k.
22. T.N. Boronina, L. Dieken, I. Lagadic, K.J. Klabunde, Zinc-silver, zinc-palladium, and zinc-gold as bimetallic systems for carbon tetrachloride dechlorination in Water. J. Hazard. Subst. Res. 1 (1998) 1–23. https://doi.org/10.4148/1090-7025.1006.
23. P. Srinoi, Y.T. Chen, V. Vittur, M.D. Marquez, T.R. Lee, Bimetallic nanoparticles: enhanced magnetic and optical properties for emerging biological applications. Appl. Sci. 8 (2018) 1106. https://doi.org/10.3390/app8071106.
24. R.K. Gautam, V. Rawat, S. Banerjee, M.A. Sanroman, S. Soni, S.K. Singh, M.C. Chattopadhyaya, Synthesis of bimetallic Fe–Zn nanoparticles and its application towards adsorptive removal of carcinogenic dye malachite green and Congo red in water. J. Mol. Liq. 212 (2015) 227–236. https://doi.org/10.1016/j.molliq.2015.09.006.

© 2025 by the author(s). Distributed under a Creative Commons CC BY license.

Preprints.org (www.preprints.org) | NOT PEER-REVIEWED | Posted: 4 November 2025 doi:10.20944/preprints202511.0036.v1

25. T. Wang, J. Su, X. Jin, Z. Chen, M. Megharaj, R. Naidu, Functional clay supported bimetallic nZVI/Pd nanoparticles used for removal of methyl orange from aqueous solution. J. Hazard. Mater. 262 (2013) 819–825. https://doi.org/10.1016/j.jhazmat.2013.09.028.
26. Z. Marková, K.M.H. Šišková, J. Filip, J. Čuda, M. Kolář, K. Šafářová, I. Medřík, R. Zbořil, Air stable magnetic bimetallic Fe−Ag nanoparticles for advanced antimicrobial treatment and phosphorus removal. Environ. Sci. Technol. 47 (2013) 5285–5293. https://doi.org/10.1021/es304693g.
27. J. Wang, C. Liu, L. Tong, J. Li, R. Luo, J. Qi, Y. Li, L. Wang, Iron–copper bimetallic nanoparticles supported on hollow mesoporous silica spheres: an effective heterogeneous Fenton catalyst for orange II degradation. RSC Adv. 5 (2015) 69593–69605. https://doi.org/10.1039/c5ra10826h.
28. N. Basavegowda, K. Mishra, Y.R. Lee, Trimetallic FeAgPt alloy as a nanocatalyst for the reduction of 4-nitroaniline and decolorization of rhodamine B: A comparative study. J. Alloys Compd. 701 (2017) 456–464. https://doi.org/ 10.1016/j.jallcom.2017.01.122.
29. A. Roy, S. Kunwar, U. Bhusal, D.S. Idris, S. Alghamdi, K. Chidambaram, A.A. Qureshi, N.F. Qusty, A.A. Khan, K. Kaur, A. Roy, Dye degradation activity of biogenically synthesized Cu/Fe/Ag trimetallic nanoparticles. Green Process. Synth. 13 (2024) 1–12. https://doi.org/10.1515/gps-2023-0267.
30. Z. Khan, Trimetallic nanoparticles: Synthesis, characterization and catalytic degradation of formic acid for hydrogen generation. Int. J. Hydrogen Energy 44 (2019) 11503–11513. https://doi.org/10.1016/j.ijhydene.2019.03.122.
31. Y. Yuan, D. Yuan, Y. Zhang, B. Lai, Exploring the mechanism and kinetics of Fe-Cu-Ag trimetallic particles for p-nitrophenol reduction. Chemosphere 186 (2017) 132–139. https://doi.org/10.1016/j.chemosphere.2017.07.038.
32. M. Kgatle, K. Sikhwivhilu, G. Ndlovu, N. Moloto, Degradation kinetics of methyl orange dye in water using trimetallic Fe/Cu/Ag nanoparticles. Catalysts 11 (2021) 428. https://doi.org/10.3390/catal11040428.
33. M. Rabiei, A. Palevicius, A. Monshi, S. Nasiri, A. Vilkauskas, G. Janusas, Comparing methods for calculating nano crystal size of natural hydroxyapatite using x-ray diffraction. Nanomaterials 10 (2020) 1–21. https://doi.org/10.3390/nano10091627.
34. M. Boudart, Turnover rates in heterogeneous catalysis. Chem. Rev. 95 (1995) 661–666. https://doi.org/10.1021/cr00035a009.
35. C.A. Ruiz-Torres, R.F. Araujo-Martínez, G.A. Martínez-Castañón, J.E. Morales-Sánchez, J.M. Guajardo-Pacheco, J. González-Hernández, T.J. Lee, H.S. Shin, Y. Hwang, F. Ruiz, Preparation of air stable nanoscale zero valent iron functionalized by ethylene glycol without inert condition. Chem. Eng. J. 336 (2018) 112–122. https://doi.org/10. 1016/j.cej.2017.11.047.
36. J.P. Dhal, B.G. Mishra, G. Hota, Hydrothermal synthesis and enhanced photocatalytic activity of ternary Fe_2O_3/$ZnFe_2O_4$/ZnO nanocomposite through cascade electron transfer. RSC Adv. 5 (2015) 58072–58083. https://doi.org/10.1039/c5ra05894e.
37. J. Wang, C. Liu, I. Hussain, C. Li, J. Li, X. Sun, J. Shen, W. Han, L. Wang, Iron–copper bimetallic nanoparticles supported on hollow mesoporous silica spheres: the effect of Fe/Cu ratio on heterogeneous Fenton degradation of a dye. RSC Adv. 6 (2016) 54623–54635. https://doi.org/10.1039/c6ra08501f.
38. X. Weng, Z. Chen, Z. Chen, M. Megharaj, Clay supported bimetallic Fe/Ni nanoparticles used for reductive degradation of amoxicillin in aqueous solution: Characterization and kinetics. Colloids Surfaces A Physicochem. Eng. Asp. 443 (2014) 404–409. https://doi.org/10.1016/j.colsurfa.2013.11.047.
39. T. Zhou, Y. Li, T.T. Lim, Catalytic hydrodechlorination of chlorophenols by Pd/Fe nanoparticles: Comparisons with other bimetallic systems, kinetics and mechanism. Sep. Purif. Technol. 76 (2010) 206–214. https://doi.org/10.1016/j.seppur.2010.10.010.
40. Z. Fang, X. Qiu, J. Chen, X. Qiu, Debromination of polybrominated diphenyl ethers by Ni/Fe bimetallic nanoparticles: Influencing factors, kinetics, and mechanism. J. Hazard. Mater. 185 (2011) 958–969. https://doi.org/10.1016/j.jhazmat.2010.09.113.
41. C.A. Ruiz-Torres, R.F. Araujo-Martínez, G.A. Martínez-Castañón, J.E. Morales-Sánchez, T.J. Lee, H.S. Shin, Y. Hwang, A. Hurtado-Macías, F. Ruiz, A cost-effective method to prepare size-controlled nanoscale zero-valent iron for nitrate reduction. Environ. Eng. Res. 24 (2019) 463–473. https://doi.org/10.4491/eer.2018.320.

© 2025 by the author(s). Distributed under a Creative Commons CC BY license.

Preprints.org (www.preprints.org) | NOT PEER-REVIEWED | Posted: 4 November 2025 doi:10.20944/preprints202511.0036.v1

42. P. Scardi, M. Leoni, K.R. Beyerlein, On the modelling of the powder pattern from a nanocrystalline material. Zeitschrift Fur Krist. 226 (2011) 924–933. https://doi.org/10.1524/zkri.2011.1448.
43. K. Shameli, M. Bin Ahmad, A. Zamanian, P. Sangpour, P. Shabanzadeh, Y. Abdollahi, M. Zargar, Green biosynthesis of silver nanoparticles using *Curcuma longa* tuber powder. Int. J. Nanomedicine 7 (2012) 5603–5610. https://doi.org/10.2147/IJN.S36786.
44. K. A. Abdullah, S. Awad, J. Zaraket, C. Salame, Synthesis of ZnO nanopowders by using Sol-gel and studying their structural and electrical properties at different temperature. Energy Procedia 119 (2017) 565–570. https://doi.org/10.1016/j.egypro.2017.07.080.
45. H. Wasly, X-Ray analysis for determination the crystallite size and lattice strain in ZnO nanoparticles. J. Al-Azhar Univ. Eng. Sect. 13 (2018) 1312–1320. https://doi.org/10.21608/auej.2018.18943.
46. P. Vanysek, Electrode Potentials. CRC Handbook of Chemistry and Physics, 92nd Edition, 1982.
47. S. Mülhopt, S. Diabaté, M. Dilger, C. Adelhelm, C. Anderlohr, T. Bergfeldt, J.G. de la Torre, Y. Jiang, E. Valsami-Jones, D. Langevin, I. Lynch, E. Mahon, I. Nelissen, J. Piella, V. Puntes, S. Ray, R. Schneider, T. Wilkins, C. Weiss, H.R. Paur, Characterization of nanoparticle batch-to-batch variability. Nanomaterials 8 (2018). https://doi.org/10.3390/nano8050311.
48. Y. Zhang, Y. Su, X. Zhou, C. Dai, A.A. Keller, A new insight on the core–shell structure of zerovalent iron nanoparticles and its application for Pb(II) sequestration. J. Hazard. Mater. 263 (2013) 685– 693. https://doi.org/10.1016/j.jhazmat.2013.10.031.
49. Y. Liang, C.-C. Wang, Surface crystal feature-dependent photoactivity of ZnO–ZnS composite rods *via* hydrothermal sulfidation. RSC Adv. 8 (2018) 5063–5070. https://doi.org/10.1039/c7ra13061a.
50. N.T. Mai, T.T. Thuy, D.M. Mott, S. Maenosono, Chemical synthesis of blue-emitting metallic zinc nano-hexagons. CrystEngComm 15 (2013) 6606. https://doi.org/10.1039/c3ce40801a.
51. N.M. Shamhari, B.S. Wee, S.F. Chin, K.Y. Kok, Synthesis and characterization of zinc oxide nanoparticles with small particle size distribution. Acta Chim. Slov. 65 (2018) 578–585. https://doi.org/10.17344/acsi.2018.4213.
52. M.T. Zin, J. Borja, H. Hinode, W. Kurniawan, Synthesis of bimetallic fe/cu nanoparticles with different copper loading ratios. Int. J. Chem. Nucl. Metall. Mater. Eng. 7 (2013) 669–673. https://doi.org/10.5281/zenodo.1336236.
53. R. Sharma, A. Dhillon, D. Kumar, Mentha-Stabilized silver nanoparticles for high-performance colorimetric detection of Al(III) in aqueous systems. Sci. Rep. 8 (2018) 1–13. https://doi.org/10.1038/s41598-018-23469-1.
54. J. Trujillo-Reyes, V. Sánchez-Mendieta, A. Colín-Cruz, R.A. Morales-Luckie, Removal of indigo blue in aqueous solution using Fe/Cu nanoparticles and C/Fe–Cu nanoalloy composites. Water. Air. Soil Pollut. 207 (2010) 307–317. https://doi.org/10.1007/s11270-009-0138-1.
55. S. Luo, S. Yang, X. Wang, C. Sun, Reductive degradation of tetrabromobisphenol using Iron–Silver and Iron–Nickel bimetallic nanoparticles with microwave energy. Environ. Eng. Sci. 29 (2012) 453–460. https://doi.org/10.1089/ees.2010.0376.
56. S. Mossa Hosseini, B. Ataie-Ashtiani, M. Kholghi, Nitrate reduction by nano-Fe/Cu particles in packed column. Desalination 276 (2011) 214–221. https://doi.org/10.1016/j.desal.2011.03.051.
57. K.J. Carroll, D.M. Hudgins, S. Spurgeon, K.M. Kemner, B. Mishra, M.I. Boyanov, L.W. Brown, M.L. Taheri, E.E. Carpenter, One-pot aqueous synthesis of Fe and Ag core/shell nanoparticles. Chem. Mater. 22 (2010) 6291–6296. https://doi.org/10.1021/cm101996u.
58. W.J. Tseng, Y.-C. Chuang, Chemical Preparation of Bimetallic Fe/Ag core/shell composite nanoparticles. J. Nanosci. Nanotechnol. 18 (2017) 2790–2796. https://doi.org/10.1166/jnn.2018.14351.
59. M. Fiedot, O. Rac, P. Suchorska-Woźniak, I. Karbownik, H. Teterycz, Polymer-surfactant interactions and their influence on zinc oxide nanoparticles morphology. Manuf. Nanostructures (2014) 108–128.
60. S.N. Zhu, G. hua Liu, K.S. Hui, Z. Ye, K.N. Hui, A facile approach for the synthesis of stable amorphous nanoscale zero-valent iron particles. Electron. Mater. Lett. 10 (2014) 143–146. https://doi.org/10.1007/s13391-013-2123-5.
61. W. Liang, C. Dai, X. Zhou, Y. Zhang, Application of zero-valent iron nanoparticles for the removal of aqueous zinc ions under various experimental conditions. PLoS One 9 (2014) e85686. https://doi.org/10.1371/journal.pone.0085686.

© 2025 by the author(s). Distributed under a Creative Commons CC BY license.

Preprints.org (www.preprints.org) | NOT PEER-REVIEWED | Posted: 4 November 2025 doi:10.20944/preprints202511.0036.v1

62. R.P.P. Singh, I.S. Hudiara, S.B. Rana, Effect of calcination temperature on the structural, optical and magnetic properties of pure and Fe-doped ZnO nanoparticles. Mater. Sci. Pol. 34 (2016) 451–459. https://doi.org/10.1515/msp-2016-0059.
63. B. Akbari, M.P. Tavandashti, M. Zandrahimi, Particle size characterization of nanoparticles: A practical approach. Iran. J. Mater. Sci. Eng. 8 (2011) 48–56.
64. A. Ruys, Processing, Structure, and Properties of Alumina Ceramics, Alumina Ceramics: Biomedical and clinical applications. First edition, Woodhead Publishing, Sawston, United Kingdom, 2019, pp. 71-121.
65. T.A. Tengku Sallehudin, M.N. Abu Seman, S.M.S. Tuan Chik, Preparation and characterization silver nanoparticle embedded polyamide nanofiltration (NF) membrane. MATEC Web Conf. 150 (2018) 02003. https://doi.org/10. 1051/matecconf/201815002003.
66. G. Li, R. Jin, Catalysis by gold nanoparticles: carbon-carbon coupling reactions. Nanotechnol. Rev. 2 (2013) 529–545. https://doi.org/10.1515/ntrev-2013-0020.
67. K.H. Kumar, N. Venkatesh, H. Bhowmik, A. Kuila, Metallic nanoparticle: A review. Biomed. J. Sci. Tech. Res. 4 (2018) 3765–3775. https://doi.org/10.26717/BJSTR.2018.04.001011.
68. S.J. Bransfield, D.M. Cwiertny, K. Livi, D.H. Fairbrother, Influence of transition metal additives and temperature on the rate of organohalide reduction by granular iron: implications for reaction mechanisms. Appl. Catal. B Environ. 76 (2007) 348–356. https://doi.org/10.1016/j.apcatb.2007.06.003.
69. S.S. Zhang, N. Yang, S.Q. Ni, V. Natarajan, H.A. Ahmad, S. Xu, X. Fang, J. Zhan, One-pot synthesis of highly active Ni/Fe nanobimetal by simultaneous ball milling and in situ chemical deposition. RSC Adv. 8 (2018) 26469–26475. https://doi.org/10.1039/c8ra04426k.
70. X. Chen, D. Ji, X. Wang, L. Zang, Review on Nano zerovalent Iron (nZVI): From modification to environmental applications. IOP Conf. Ser. Earth Environ. Sci. 51 (2017) 012004. https://doi.org/10.1088/1755-1315/51/1/012004.
71. A. Ghauch, H.A. Assi, H. Baydoun, A.M. Tuqan, A. Bejjani, Fe^0-based trimetallic systems for the removal of aqueous diclofenac: Mechanism and kinetics. Chem. Eng. J. 172 (2011) 1033–1044. https://doi.org/10.1016/j.cej.2011.07.020.
72. L.P. Zhu, B.K. Zhu, L. Xu, Y.X. Feng, F. Liu, Y.Y. Xu, Corona-induced graft polymerization for surface modification of porous polyethersulfone membranes. Appl. Surf. Sci. 253 (2007) 6052–6059. https://doi.org/10.1016/j.apsusc.2007.01.004.
73. Y. Gao, F. Wang, Y. Wu, R. Naidu, Z. Chen, Comparison of degradation mechanisms of microcystin-LR using nanoscale zero-valent iron (nZVI) and bimetallic Fe/Ni and Fe/Pd nanoparticles. Chem. Eng. J. 285 (2016) 459–466. https://doi.org/10.1016/j.cej.2015.09.078.
74. R. Rodrigues, S. Betelu, S. Colombano, G. Masselot, T. Tzedakis, I. Ignatiadis, Reductive dechlorination of hexachlorobutadiene by a Pd/Fe microparticle suspension in dissolved lactic acid polymers: Degradation mechanism and kinetics. Ind. Eng. Chem. Res. 56 (2017) 12092–12100. https://doi.org/10.1021/acs.iecr.7b03012.
75. G.G. Muradova, S.R. Gadjieva, L. Di Palma, G. Vilardi, Nitrates removal by bimetallic nanoparticles in water. Chem. Eng. Trans. 47 (2016) 205–210. https://doi.org/10.3303/CET1647035.
76. F. Parvin, O.K. Nayna, S.M. Tareq, S.Y. Rikta, A.K. Kamal, Facile synthesis of iron oxide nanoparticle and synergistic effect of iron nanoparticle in the presence of sunlight for the degradation of DOM from textile wastewater. Appl. Water Sci. 8 (2018) 1–11. https://doi.org/10.1007/s13201-018-0719-5.
77. D.F. Paris, W.C. Steen, G.L. Baughman, J.T. Barnett, Second-Order model to predict microbial degradation of organic compounds in natural waters. Appl. Environ. Microbiol. 41 (1981) 603–609. https://doi.org/10.1128/aem.41.3.603-609.1981.
78. K.V.G. Ravikumar, S. Dubey, M. pulimi, N. Chandrasekaran, A. Mukherjee, Scale-up synthesis of zero-valent iron nanoparticles and their applications for synergistic degradation of pollutants with sodium borohydrideJ. Mol. Liq. 224 (2016) 589–598. https://doi.org/10.1016/j.molliq.2016.10.040.
79. Z.X. Chen, X.Y. Jin, Z. Chen, M. Megharaj, R. Naidu, Removal of methyl orange from aqueous solution using bentonite-supported nanoscale zero-valent iron. J. Colloid Interface Sci. 363 (2011) 601–607. https://doi.org/10.1016/j.jcis.2011.07.057.

© 2025 by the author(s). Distributed under a Creative Commons CC BY license.

Preprints.org (www.preprints.org) | NOT PEER-REVIEWED | Posted: 4 November 2025 doi:10.20944/preprints202511.0036.v1

80. L. Han, S. Xue, S. Zhao, J. Yan, L. Qian, M. Chen, Biochar supported nanoscale iron particles for the efficient removal of methyl orange dye in aqueous solutions. PLoS One 10 (2015) 1–15. https://doi.org/10.1071/journal.pone.0132967.
81. A.D. Bokare, R.C. Chikate, C. V. Rode, K.M. Paknikar, Effect of surface chemistry of Fe-Ni nanoparticles on mechanistic pathways of azo dye degradation. Environ. Sci. Technol. 41 (2007) 7437–7443. https://doi.org/10.1021/es071107q.
82. C.J. Lin, S.L. Lo, Y.H. Liou, Dechlorination of trichloroethylene in aqueous solution by noble metal-modified iron. J. Hazard. Mater. 116 (2004) 219–228. https://doi.org/10.1016/j.jhazmat.2004.09.005.
83. H.L. Lien, W. Zhang, Enhanced dehalogenation of halogenated methanes by bimetallic Cu/Al. Chemosphere 49 (2002) 371–378. https://doi.org/10.1016/S0045-6535(02)00248-5.
84. L.G. Devi, R. Shyamala, Photocatalytic activity of SnO_2-α-Fe_2O_3 composite mixtures: Exploration of number of active sites, turnover number and turnover frequency. Mater. Chem. Front. 2 (2018) 796–806. https://doi.org/10.1039/c7qm00536a.
85. S.A. Kondrat, J.A. van Bokhoven, A perspective on counting catalytic active sites and rates of reaction using X-ray spectroscopy. Top. Catal. 62 (2019) 1218–1227. https://doi.org/10.1007/s11244-018-1057-4.
86. S. Navalon, D. Amarajothi, A. Mercedes, M. Antonietti, H. Garcia, Active sites on graphene-based materials as metal-free catalysts. Chem. Soc. Rev. 46 (2017) 4501–4529. https://doi.org/10.1039/c7cs00156h.
87. J.D. Benck, T.R. Hellstern, J. Kibsgaard, P. Chakthranont, T.F. Jaramillo, Catalyzing the hydrogen evolution reaction (HER) with molybdenum sulfide nanomaterials. ACS Catal. 4 (2014) 3957–3971. https://doi.org/10.1021/cs500923c.
88. N. Sobana, M. Swaminathan, The effect of operational parameters on the photocatalytic degradation of acid red 18 by ZnO. Sep. Purif. Technol. 56 (2007) 101–107. https://doi.org/10.1016/j.seppur.2007.01.032.
89. I. Poulios, I. Tsachpinis, Photodegradation of the textile dye Reactive Black 5 in the presence of semiconducting oxides. J. Chem. Technol. Biotechnol. 74 (1999) 349–357. https://doi.org/10.1002/(SICI)1097-4660(199904)74:4<349::AID-JCTB5>3.0.CO;2-7.
90. F. Rezaei, D. Vione, Effect of pH on zero valent iron performance in heterogeneous Fenton and Fenton-like processes: A review. Molecules 23 (2018). https://doi.org/10.3390/molecules23123127.
91. Y.H. Shih, C.P. Tso, L.Y. Tung, Rapid degradation of methyl orange with nanoscale zerovalent iron particles. Sustain. Environ. Res. 20 (2010) 137–143.
92. N.A. Youssef, S.A. Shaban, F.A. Ibrahim, A.S. Mahmoud, Degradation of methyl orange using Fenton catalytic reaction. Egypt. J. Pet. 25 (2016) 317–321. https://doi.org/10.1016/j.ejpe.2015.07.017.
93. P. Niu, Photocatalytic Degradation of methyl orange in aqueous TiO_2 Suspensions. Asian J. Chem. 25 (2013) 1103–1106. https://doi.org/10.14233/ajchem.2013.13539.
94. S. Luo, S. Yang, X. Wang, C. Sun, Reductive degradation of tetrabromobisphenol A over iron–silver bimetallic nanoparticles under ultrasound radiation. Chemosphere 79 (2010) 672–678. https://doi.org/10.1016/j.chemosphere.2010.02.011.
95. J. Singh, Y.Y. Chang, J.R. Koduru, J.K. Yang, D.P. Singh, Rapid Fenton-like degradation of methyl orange by ultrasonically dispersed nano-metallic particles. Environ. Eng. Res. 22 (2017) 245–254. https://doi.org/10.4491/eer.2016.138.
96. E.M. El-Sayed, M.F. Elkady, M.M.A. El-Latif, Biosynthesis and characterization of zerovalent iron nanoparticles and its application in azo dye degradation. Indian J. Chem. Technol. 24 (2017) 541–547.
97. T. Chen, Y. Zheng, J.M. Lin, G. Chen, Study on the photocatalytic degradation of methyl orange in water using Ag/ZnO as catalyst by liquid chromatography electrospray ionization ion-trap mass spectroscopy. J. Am. Soc. Mass Spectrom. 19 (2008) 997–1003. https://doi.org/10.1016/j.jasms.2008.03.008.
98. T. Shen, C. Jiang, C. Wang, J. Sun, X. Wang, X. Li, TiO_2 modified abiotic-biotic process for the degradation of azo dye methyl orange. RSC Adv. 5 (2015) 58704–58712. https://doi.org/10.1039/c5ra06686g.
99. S. Xie, P. Huang, J.J. Kruzic, X. Zeng, H. Qian, A highly efficient degradation mechanism of methyl orange using Fe-based metallic glass powders. Sci. Rep. 6 (2016) 1–10. https://doi.org/10.1038/srep21947.
100. K. Dai, H. Chen, T. Peng, D. Ke, H. Yi, Photocatalytic degradation of methyl orange in aqueous suspension of mesoporous titania nanoparticles. Chemosphere 69 (2007) 1361–1367. https://doi.org/10.1016/j.chemosphere.2007.05.021.

© 2025 by the author(s). Distributed under a Creative Commons CC BY license.

Preprints.org (www.preprints.org) | NOT PEER-REVIEWED | Posted: 4 November 2025 doi:10.20944/preprints202511.0036.v1

101. Q.B. Nguyen, D.P. Vu, T.H.C. Nguyen, T.D. Doan, N.C. Pham, T.L. Duong, D.L. Tran, G.L. Bach, H.C. Tran, N.N. Dao, Photocatalytic activity of $BiTaO_4$ Nanoparticles for the degradation of methyl orange under visible light. J. Electron. Mater. 48 (2019) 3131–3136. https://doi.org/10.1007/s11664-019-07066-0.
102. B. Lai, Q. Ji, Y. Yuan, D. Yuan, Y. Zhou, J. Wang, Degradation of ultrahigh concentration pollutant by Fe/Cu bimetallic system at high operating temperature. Korean J. Chem. Eng. 33 (2016) 207–215. https://doi.org/10.1007/s11814-015-0135-6.
103. H.M.D.R. Herath, P.N. Shaw, P. Cabot, A.K. Hewavitharana, Effect of ionization suppression by trace impurities in mobile phase water on the accuracy of quantification by high-performance liquid chromatography/mass spectrometry. Rapid Commun. Mass Spectrom. 24 (2010) 1502–1506. https://doi.org/10.1002/rcm.4549.
104. H.J. Lu, J.K. Wang, S. Ferguson, T. Wang, Y. Bao, H.X. Hao, Mechanism, Synthesis and Modification of nano zerovalent iron in water treatment. Nanoscale 8 (2016) 9962–9975. https://doi.org/10.1039/C6NR00740F.
105. H. Lu, J. Wang, M. Stoller, T. Wang, Y. Bao, H. Hao, An overview of nanomaterials for water and wastewater treatment: Review. Adv. Mater. Sci. Eng. 2016 (2016) 4964828. https://doi.org/10.1155/2016/4964828.
106. P.G. Tratnyek, A.J. Salter, J.T. Nurmi, V. Sarathy, Environmental applications of zerovalent metals: Iron vs. Zinc. ACS Symp. Ser. 1045 (2010) 165–178. https://doi.org/10.1021/bk-2010-1045.ch009.
107. B. Kakavandi, A. Takdastan, S. Pourfadakari, M. Ahmadmoazzam, S. Jorfi, Heterogeneous catalytic degradation of organic compounds using nanoscale zero-valent iron supported on kaolinite: Mechanism, kinetic and feasibility studies. J. Taiwan Inst. Chem. Eng. 96 (2019) 329–340. https://doi.org/10.1016/j.jtice.2018.11.027.
108. A.D. Bokare, R.C. Chikate, C. V Rode, K.M. Paknikar, Iron-nickel bimetallic nanoparticles for reductive degradation of azo dye Orange G in aqueous solution. Appl. Catal. B: Environ. 79 (2008) 270–278. https://doi.org/10.1016/j.apcatb.2007.10.033.
109. J. Cao, L. Wei, Q. Huang, L. Wang, S. Han, Reducing degradation of azo dye by zero-valent iron in aqueous solution. Chemosphere 38 (1999) 565–571. https://doi.org/10.1016/s0045-6535(98)00201-x.
110. T. Raychoudhury, T. Scheytt, Potential of zerovalent iron nanoparticles for remediation of environmental organic contaminants in water: A review. Water Sci. Technol. 68 (2013) 1425–1439. https://doi.org/10.2166/wst.2013.358.

Disclaimer/Publisher's Note: The statements, opinions and data contained in all publications are solely those of the individual author(s) and contributor(s) and not of MDPI and/or the editor(s). MDPI and/or the editor(s) disclaim responsibility for any injury to people or property resulting from any ideas, methods, instructions or products referred to in the content.

© 2025 by the author(s). Distributed under a Creative Commons CC BY license.